Article

Cell Reports

IL-4Rα-Expressing B Cells Are Required for CXCL13 Production by Fibroblastic Reticular Cells

Graphical Abstract

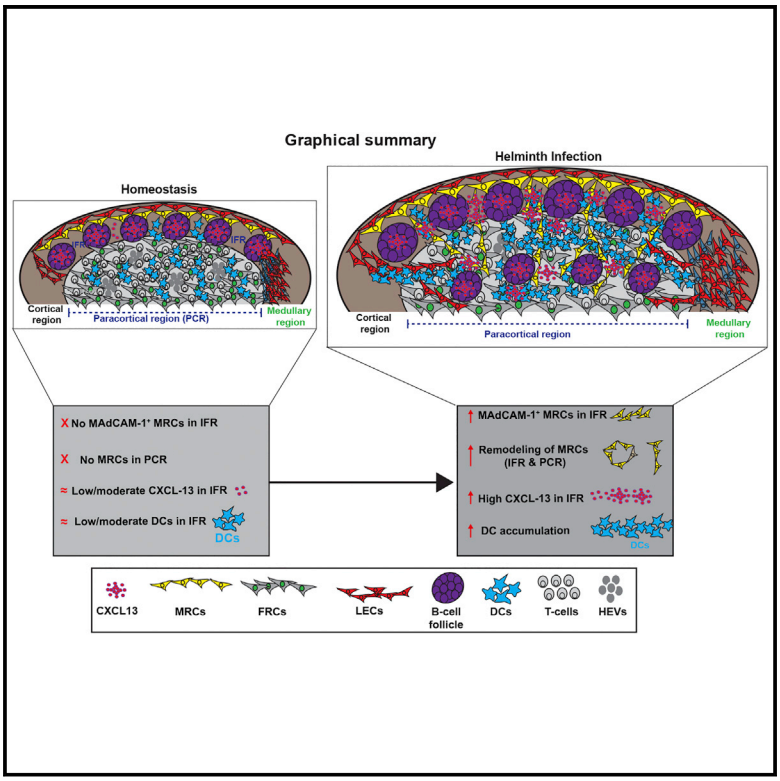

Highlights

- Helminth infection increases the number of MRCs producing CXCL13
- MRC-like cells invade B cell follicles and populate the mLN interfollicular regions
- IL-4Rα signaling to B cells promotes expansion and appearance of MRC-like cells

Authors

Lalit Kumar Dubey, Burkhard Ludewig, Sanjiv A. Luther, Nicola L. Harris

Correspondence

lalitkumar.dubey@unil.ch (L.K.D.), nicola.harris@monash.edu (N.L.H.)

In Brief

MRCs are a specialized, CXCL13-producing, stromal population located beneath the subcapsular sinus of lymph nodes. Dubey et al. demonstrate that intestinal helminth infection drives the remodeling and development of MRCs toward the paracortical region within the draining mLNs and requires the expression of type 2 cytokines and intimate B cell-stromal cell interactions.

Dubey et al., 2019, Cell Reports *27*, 2442–2458
May 21, 2019
https://doi.org/10.1016/j.celrep.2019.04.079

CellPress

OPEN ACCESS
CellPress

Cell Reports
Article

IL-4Rα-Expressing B Cells Are Required for CXCL13 Production by Fibroblastic Reticular Cells

Lalit Kumar Dubey,[1,*] Burkhard Ludewig,[2] Sanjiv A. Luther,[1,5] and Nicola L. Harris[3,4,5,6,*]
[1]Department of Biochemistry, University of Lausanne, Lausanne, Switzerland
[2]Institute of Immunobiology, Kantonsspital St. Gallen, St. Gallen, Switzerland
[3]Global Health Institute, School of Life Sciences, École Polytechnique Fédérale de Lausanne (EPFL), Lausanne, Switzerland
[4]Department of Immunology and Pathology, Central Clinical School, Monash University, The Alfred Centre, Melbourne, VIC, Australia
[5]These authors contributed equally
[6]Lead Contact
*Correspondence: lalitkumar.dubey@unil.ch (L.K.D.), nicola.harris@monash.edu (N.L.H.)
https://doi.org/10.1016/j.celrep.2019.04.079

SUMMARY

Adaptive type 2 immune responses against the intestinal helminth *Heligmosomoides polygyrus (Hp)* require the interaction of follicle-associated CXCR5$^+$ dendritic cells with naive T cells in the draining mesenteric lymph nodes (mLNs). However, the source of CXCL13 responsible for attracting CXCR5$^+$ dendritic cells has remained unclear. Using multiplex imaging combined with deep tissue analysis, we observed new CXCL13$^+$ fibroblastic reticular cells surrounding paracortical and cortical B cell follicles in the mLNs of infected mice. CXCL13$^+$ fibroblasts expressed markers of marginal reticular cells (MRCs), and their expansion required lymphotoxin (LT)-dependent interactions between IL-4Rα-expressing B cells and CCL19$^+$ fibroblasts. Infection-induced follicles did not necessarily contain follicular dendritic cells (FDCs), indicating that CXCL13$^+$ fibroblasts may instead drive their formation. These data reveal a role for lymphotoxin signaling to CCL19$^+$ fibroblasts in the development of CXCL13$^+$ MRC-like cells and adaptive type 2 immunity in response to helminth infection.

INTRODUCTION

Lymph nodes (LNs) are highly organized structures made up of hematopoietic and non-hematopoietic cells (referred to as stromal cells) that provide basic infrastructure and form specialized niches that support T and B cell responses. Stromal cells are broadly differentiated by the surface expression of podoplanin and the endothelial cell marker CD31. Non-endothelial cells are commonly referred to as fibroblastic reticular cells (FRCs) and can be separated into various subpopulations that reside in anatomically distinct regions and actively segregate T and B lymphocytes into distinct compartments (Fletcher et al., 2015; Junt et al., 2008; Mueller and Germain, 2009). FRCs that reside in the T cell-rich paracortical region are podoplanin$^+$ (PDPN$^+$), secrete CCL19/CCL21 to attract CCR7 expressing dendritic cells (DCs) and naive T cells, and are tightly associated with extracellular matrix fibers that are ER-TR7$^+$ and laminin$^+$. Those located immediately beneath the subcapsular sinus (SCS) express mucosal addressin cellular adhesion molecule-1 (MAdCAM-1), tumor necrosis factor (TNF)-related activation-induced cytokine (also known as TRANCE/CD254/RANKL), and the B cell chemoattractant CXCL13 (Hoorweg et al., 2015; Katakai et al., 2008; Magri et al., 2014), and are commonly referred to as marginal reticular cells (MRCs). However, the role of MRCs during homeostasis and inflammatory conditions remain largely unknown, especially in relation to B cell follicle formation and function.

B cell follicle formation strongly depends on CXCL13. It is mainly produced by resident non-hematopoietic cells and is responsible for directing CXCR5-expressing B cells efficiently into the follicles and for forming their typical roundish shape (Ansel et al., 2002; Cyster and Schwab, 2012; Fu et al., 1998; Hardtke et al., 2005). Besides MRCs, the best known CXCL13 source is the follicular dendritic cells (FDCs), which populate the light zone of B cell follicles and expresses FDC-M1 and CD35 as cell type-specific markers. In addition, FDCs retain antigens at the cell surface over weeks or months to support affinity maturation within the germinal centers and to facilitate antibody production. FDC ablation disrupts proper B cell follicle organization and germinal center reactions, leading to high-affinity antibody generation (Aguzzi et al., 2014; Wang et al., 2011). Although the exact lineage relations between T zone FRCs, MRCs, and FDCs remain unclear, a recent study identified MRCs as possible precursors of FDCs (Jarjour et al., 2014). In this fate-mapping study, the authors show that inflammation promotes the formation of new FDCs that arise from the proliferation and differentiation of MRCs rather than from the expansion of existing FDCs. However, the triggers for MRC differentiation into FDCs were not defined (Jarjour et al., 2014). Few other non-hematopoietic CXCL13 sources have been identified in adult secondary lymphoid organs and include B zone reticular cells (BRCs) and versatile stromal cells (VSCs), which are found in the follicular mantle rather than in the follicle center (Ansel et al., 2002; Katakai et al., 2008; Mionnet et al., 2013; Cremasco et al., 2014). High endothelial venules (HEVs) within the mesenteric LN (mLN) can also serve as an arrest factor for incoming B cells by producing CXCL13, which along with other

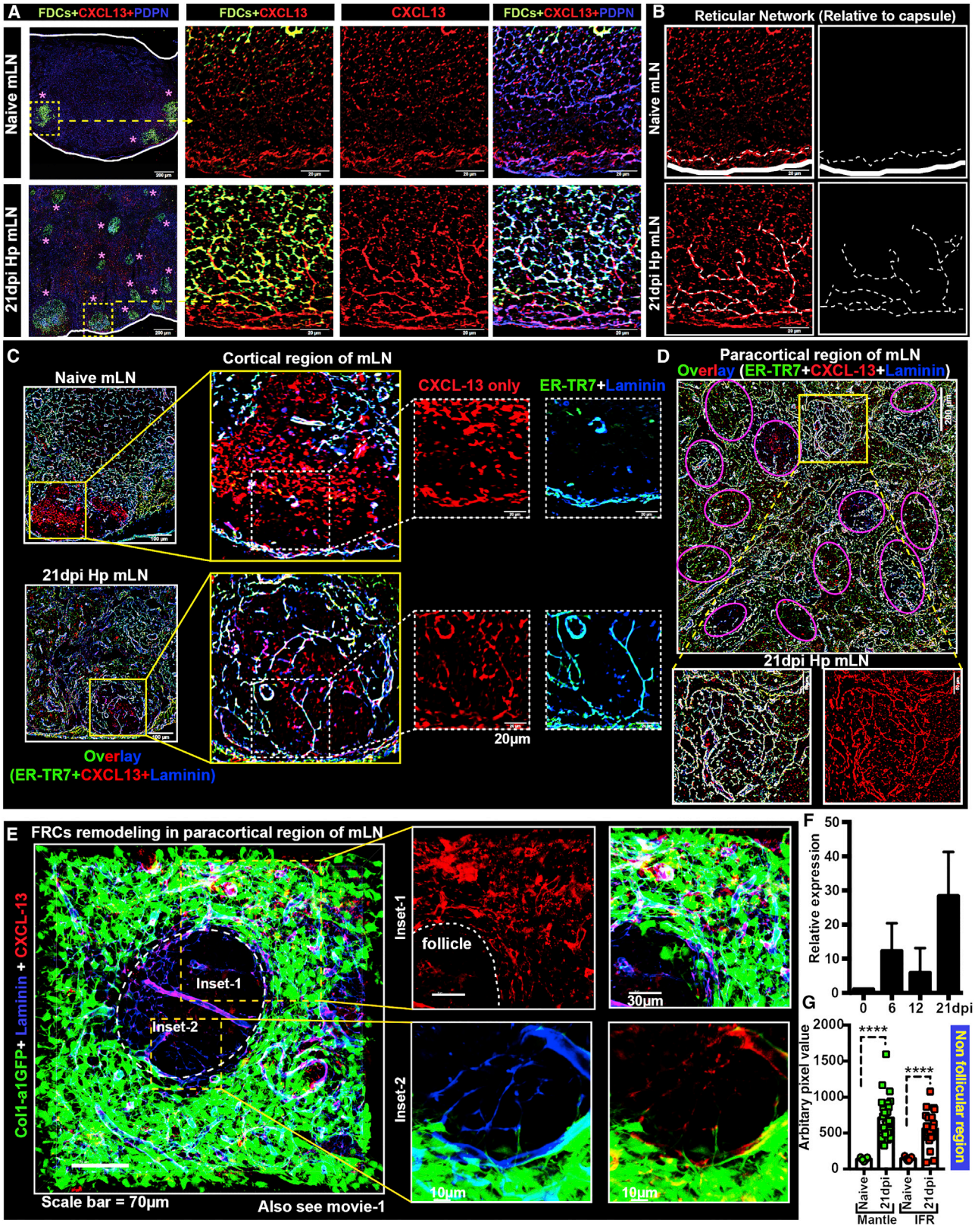

(legend on next page)

chemokines can regulate the arrest and transmigration of CXCR5$^+$ cells (Kanemitsu et al., 2005; Okada et al., 2002).

CXCL13 is important not only for the formation of proper B cell follicles but also for the embryonic development of LN anlagen, which then develops into mature secondary lymphoid organs (Ansel et al., 2002). As a consequence, CXCL13- and CXCR5-deficient mice lack most LNs (Ansel et al., 2002; Ohl et al., 2003; Luther et al., 2003). CXCL13 is mainly expressed in embryonic LN by MAdCAM-1$^+$ fibroblasts that were called lymphoid tissue organizer (LTo) cells due to their critical function in attracting and clustering CXCR5$^+$ type 3 innate lymphoid cells (ILC3) in the early LN anlagen. This CXCL13 expression is strongly dependent on lymphotoxin-$\alpha_1\beta_2$ (LT$\alpha\beta$) signals between the recruited ILC3 and resident stromal cells, including lymphotoxin β receptor$^+$ (LTβR$^+$) fibroblasts and endothelial cells, in a positive feedback loop (Fletcher et al., 2015). A similar circuit between adult B cells expressing LT$\alpha\beta$ and CXCL13$^+$ FDCs drives B cell follicle maintenance in the adult LN and spleen (Cyster, 2014). Thus, both CXCL13 and lymphotoxin have emerged as key signals in lymphoid tissue and follicle development and maintenance, with further roles in germinal center reactions. MRCs alongside B cell follicles and subcapsular macrophages were proposed to form interleukin-7$^+$ (IL-7$^+$) niches for ILC3 (Hoorweg et al., 2015). Furthermore, ILC3 trafficking to mLN was proposed to be important for mucosal immunity (Mackley et al., 2015) However, a precise understanding of the contributions of MRCs to the mucosal immune response is still lacking.

The generation of adaptive type 2 immunity in the mLN of mice infected with the intestinal helminth *Heligmosomoides polygyrus (Hp)* is also CXCL13 dependent and requires the positioning of CXCR5 expressing DCs together with T cells within the follicle mantle and interfollicular regions (IFRs) (León et al., 2012). However, the source of CXCL13, responsible for recruiting and locating the DCs, has remained unclear. We recently reported that, in the mLN of *Hp*-infected mice, interactions between lymphotoxin-expressing B cells and LTβR$^+$ FRCs promote the formation of new B cell follicles within the paracortex and that this process was necessary to support antibody production and parasite expulsion (Dubey et al., 2016). As the formation of new B cell follicles would be expected to require the development of new CXCL13-producing cells, we next set out to investigate the nature and positioning of CXCL13$^+$ cells within the mLN of *Hp*-infected mice and to further determine the factors regulating the increased expression of CXCL13. Using immunofluorescence staining, combined with deep tissue imaging and flow cytometry, we were able to demonstrate that *Hp* infection results in an extensive increase in the number of FRCs expressing a phenotype resembling the previously identified MRCs. These CXCL13$^+$ MRC-like cells were found to extend into the center of peripherally located B cell follicles and to uniquely be present in the IFRs and newly developed paracortical B cell follicles. Of note these follicles did not necessarily contain FDCs, indicating that they can form independently of FDCs. Lastly, the use of bone marrow chimeras demonstrated that the development of CXCL13$^+$ MRC-like cells required IL-4-mediated activation of B cells and B cell-FRC crosstalk via lymphotoxin-LTβR.

RESULTS

Helminth Infection Drives the Expansion of CXCL13-Producing FRCs within the Draining mLN

Mice infected with *Hp* show extensive development of new B cell follicles within draining mLN (Dubey et al., 2016). While CXCR5 is known to be important for the efficient induction of T helper 2 (Th2) cells in this model system, the cellular sources of CXCL13 involved in attracting the CXCR5$^+$ DC and T cells to IFR and in initiating and maintaining new follicular structures are not well defined (León et al., 2012). To gain insight into this question, we performed immunofluorescence staining of mLN cryosections using antibodies against B220 (to identify B cell follicles), FDC-M1/CD35 (to identify FDCs), CD11c (for DCs), and PDPN/laminin/ER-TR7 (for reticular cells and the associated matrix). These stains were combined with the detection of CXCL13, and images were taken from the SCS region in and around B cell follicles representing the follicular mantle, the IFR, and the paracortical region of mLN from naive or *Hp*-infected mice. The cortical region is defined as a capsule-associated area, while the term ''paracortex'' is used to indicate the more central regions (i.e. paracortical region) of mLN. Naive mLN exhibited clusters of FDCs located solely within the cortex, while in *Hp*-infected mLNs, FDC clusters could be observed throughout the cortical and paracortical region (or the more

Figure 1. Upon Helminth Infection, CXCL13-Expressing FRC Expand and Remodel around B Cell Follicles and in Interfollicular Regions of Draining mLNs

C57BL/6J (WT) mice were infected with *Hp* and the mLN collected at day 0 (naive) and 21 dpi and visualized using immunofluorescence microscopy.

(A) mLN sections were stained for CXCL13 expression (red), FDCs (FDC-M1$^+$, green), and fibroblastic reticular cells (PDPN$^+$, blue). Magenta stars in the left-hand overlay highlight the locations of FDCs.

(B) Higher-magnification images shown in (A) were segmented and duplicated, and the non-FDC CXCL13$^+$ reticular structures arising from the SCS were hand drawn (dashed white line) and shown on a black background for improved visualization. The capsule is highlighted using solid white lines. All of the images shown were taken from a single mouse, but are representative of three or more independent experiments. For all data shown, each independent experiment included n $\geq$ 2–3 mice per group per time point. Scale bars, 200 and 20 μm.

(C and D) mLN sections were stained for CXCL13 expression (red), ER-TR7$^+$ (green), and laminin$^+$ (blue) reticular cells to better visualize the reticular matrix network. (C) Cortical regions and (D) paracortical regions are shown at increasing magnifications, with pink circles representing follicles.

(E) Immunofluorescence analysis of *Hp*-infected Col-1a1GFP mice mLN (>100-μm-thick sections) showing paracortical FRC networks surrounding B cell follicles (green, Col-1a1GFP; red, CXCL13; blue, laminin). Col-1a1GFP$^+$Laminin$^+$CXCL13$^+$cells can be found in large numbers outside the B cell follicle. Scale bars, 70, 30, and 10 μm.

(F and G) Relative expression of mRNA encoding CXCL13 in CD45$^-$ fraction (stroma) of mLN over the indicated time course (F), and quantification of CXCL13 protein staining (pixel intensity) in the follicular mantle and interfollicular regions of images (sampled from non-follicular region; FDC-FRC networks surrounding B cell follicles) (G). Naive, n = 15; 21 dpi, n = 30. Data represent means ± SEMs. *p < 0.05 (Mann-Whitney test).

See also Video S1.

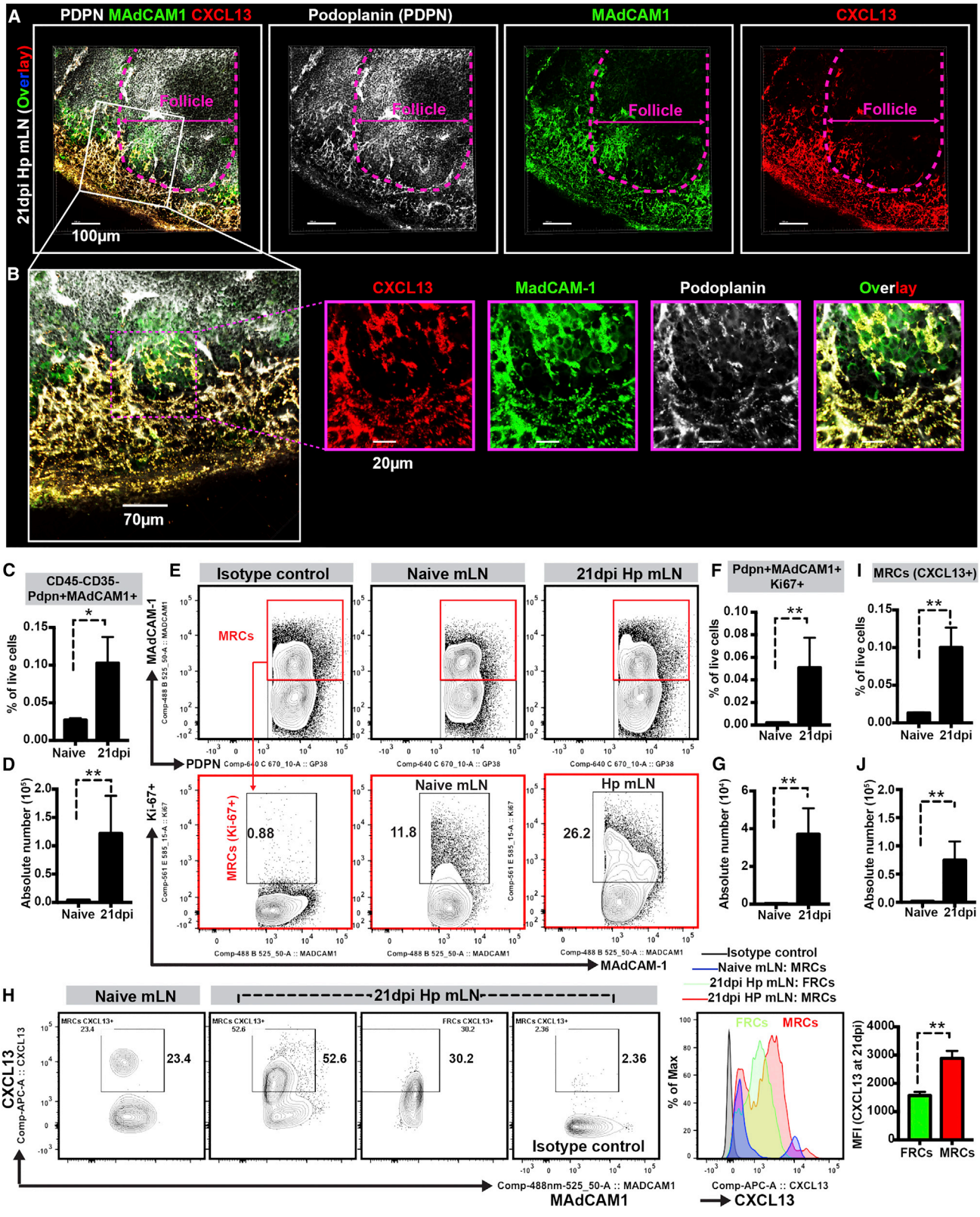

(legend on next page)

central region) (Figure 1A, magenta stars), in keeping with the expected *de novo* formation of centrally located follicles following infection (Dubey et al., 2016). However, sequential co-staining for CXCL13 and PDPN along with FDC-M1 revealed the increased presence of CXCL13$^+$ cells expressing FRC but not FDC markers (FDC-M1$^-$PDPN$^+$) within the mLNs of infected mice (Figures 1A and S1A). These cells were observed to extend their PDPN$^+$ reticular structures from the SCS region into the FDC-rich follicles located in the cortex (Figures 1A and 1B), a feature that was not observed in naive mice (Figures 1A, 1B, and S1A). The most striking CXCL13 staining was associated not with FDCs, but with the FRCs or the matrix fibers that FRCs enwrap. Of note, CXCL13 expressing reticular cells in the cortex (Figure 1C) and paracortex (Figure 1D) of *Hp*-infected mLNs were both follicular and extra-follicular in nature, while CXCL13 signals in naive mice were mainly from reticular cells in the SCS or from non-reticular cells in the follicle and were much reduced by comparison (Figure 1C). Deep tissue imaging of mLN sections obtained from *Hp*-infected Col-1a1GFP mice confirmed that although the expected CXCL13 expression by GFP$^-$ reticular cells could be observed in the central area of the activated follicle, CXCL13 expression was much more prominently found within the GFP$^+$ FRC of the follicular mantle and IFR of the paracortex (Figure 1E; Video S1). A more detailed analysis of mLNs revealed that many follicles (present in both cortical and paracortical region) did not contain CXCL13$^+$ FDCs, but instead were infiltrated by PDPN$^+$MAdCAM-1$^+$ laminin$^+$ reticular structures that extended from SCS or IFR regions into the follicles (Figures S1B and S1C; Videos S2 and S3). Based on these observations, we concluded that non-follicular reticular cells expressing CXCL13 increase in number following *Hp* infection, penetrate B cell follicles located in the cortex, and associate with newly formed follicles in the paracortex. Given the well-established role for CXCL13 in driving B cell clustering and follicle formation, these observations raise the possibility that cortical and paracortical CXCL13$^+$ reticular cells participate in or drive the previously described *de novo* generation of follicles that occurs in response to *Hp* infection (Dubey et al., 2016). Lastly, we show that infection leads to a strong increase in the expression of CXCL13 mRNA in the CD45$^-$ stromal cell fraction (Figure 1F) and of CXCL13 protein in the follicular mantle and IFR where FRC but not FDC localize (Figure 1G).

CXCL13-Producing Cells Arising within the IFRs and Paracortical Region following *Hp* Infection Express Markers of MRCs

MRCs are a PDPN$^+$MAdCAM-1$^+$CXCL13$^+$ stromal subset present in the LN cortex and located just below SCS on the backside of B cell follicles (Katakai et al., 2008). In addition, MRCs are typically defined by a combination of markers, including the matrix markers laminin and ER-TR7, which are mostly absent on FDCs, and by the high expression of receptor activator of nuclear factor κB ligand (RANKL) and MAdCAM-1. In the previous section, we observed a network of cortical laminin$^+$ER-TR7$^+$ reticular cells expressing CXCL13 but lacking FDC markers. This prompted us to further investigate whether these cells expressed markers typical of MRCs. For this purpose, we sequentially stained thin (8 μm) and thick (>40 μm) mLN sections with antibodies directed against PDPN, CXCL13 and MAdCAM-1, and CD35. Visualization, by static and deep tissue imaging, of the SCS, cortex and paracortex revealed that while cells expressing MRC surface markers were limited to the SCS in naive mice (Figure S2A), they could be found in all of these regions following *Hp* infection (Figures 2A, 2B, and S2B; Video S4). We considered reticular cells to be MRC-like when they were positive for markers such as PDPN or ER-TR7 and laminin, in addition to MAdCAM-1 plus CXCL13 (Video S5), or MAdCAM-1 plus RANKL (TRANCE). Reticular cells expressing both MAdCAM-1 and RANKL and located in the paracortical region of infected mLNs were found to form interconnected networks around the B cell follicles, preferentially within the IFR (Figure S2B, insets 3 and 4). Deep tissue imaging further confirmed that laminin$^+$ reticular cells also formed an interconnected network with laminin$^-$CD35$^+$ FDCs network within the B cell follicle, suggesting an intricate reticular network organization within the mLN (Video S6). We also used flow cytometry to provide a more quantitative analysis of MRCs-like cell numbers and proliferation within the mLNs of naive and infected mice. MRC-like cells were defined as described previously (Fletcher et al., 2011) (Figures S2C and S2D). CD45$^-$TER119$^-$CD35$^-$CD31$^-$PDPN$^+$MAdCAM-1$^+$ cells showed an increase in percentage and a >10-fold increase in numbers following infection (Figures 2C and 2D). Intracellular Ki67 staining showed that MRC-like cells actively proliferated following *Hp* infection (Figures 2E–2G). Intracellular CXCL13 staining revealed that the percentage of CXCL13$^+$ cells increased, preferentially

Figure 2. The CXCL13-Expressing FRC Subset Expanding Strongly in mLNs of *Hp*-Infected Mice Represents Mainly MAdCAM-1$^+$ MRC-like Cells

(A–H) C57BL/6J (WT) mice were infected with *Hp* and the mLN collected at day 0 (naive) and 21 dpi and either analyzed using immunofluorescence microscopy (A and B) or flow cytometry (C–H).

(A) Thick (>50 μm) mLN sections were generated with a vibratome. 3D views of WT mice mLNs at 21 dpi show CXCL13 expression (red) in MRCs expressing PDPN (gray) and MAdCAM-1 (green). The dashed magenta circle outlines the B cell follicle.

(B) The white insets from (A) are magnified and shown as an overlay. Dotted magenta square is magnified and individual and combined panels are shown. Scale bars, 100, 70, and 20 μm. See also Video S4.

(C–G) MRCs were quantified using flow cytometry by gating live cells that were TER119$^-$CD45$^-$CD35$^-$CD31$^-$Podoplanin$^+$MAdCAM-1$^+$ in WT mLN post-*Hp* infection. Histogram representing (C) percentage of live cells and (D) the absolute number of MRCs are shown. (E) FACS dot plots showing MRCs proliferation (Ki67$^+$) and histogram representing (F) percentage of live cells and (G) absolute number of proliferating MRCs (Ki67$^+$) within the mLN. Data represent means ± SEMs and are representative of three independent experiments.

(H–J) Intracellular CXCL13 expression in MRCs was quantified using flow cytometry. (H) Overlay histograms showing CXCL13 expression in naive MRCs, 21 dpi MRCs, and other FRCs are shown along with mean fluorescence intensity. Histograms representing (I) percentage of live cells and (J) absolute number of CXCL13$^+$MRCs are shown. Data represent means ± SEMs and are representative of two independent experiments, with n = 3–5 mice per group.

*$p < 0.05$ (Mann-Whitney test).

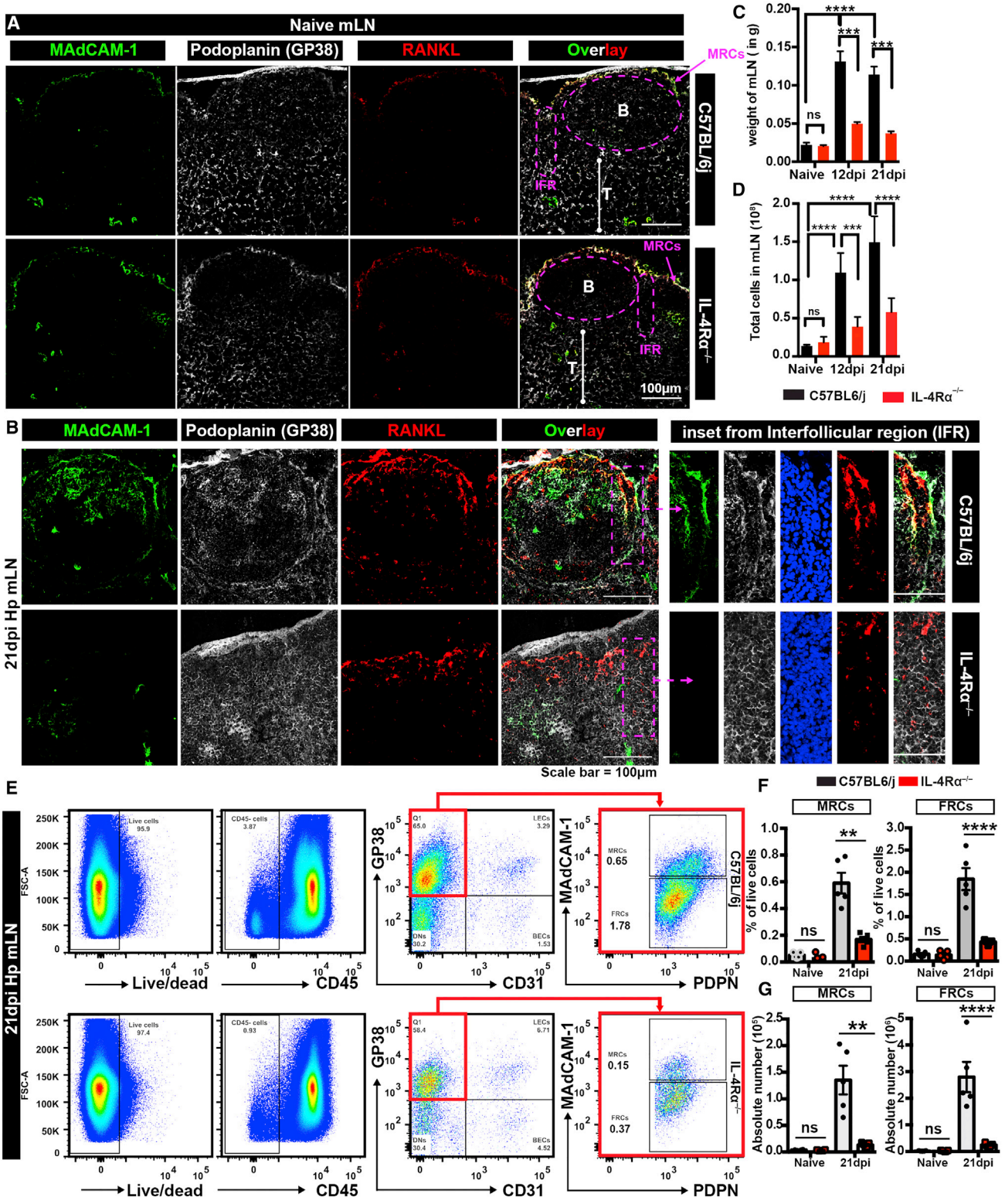

Figure 3. MRC Expansion and Remodeling in mLN of Helminth-Infected Mice Require IL-4Rα Signaling

(A–G) C57BL/6J (WT) mice and IL-4Rα-deficient (IL-4Rα$^{-/-}$) mice were infected with *Hp* and the mLNs collected at day 0 (naive) and 21 dpi and either analyzed using immunofluorescence microscopy (A and B) or flow cytometry (C–G).

(legend continued on next page)

those with the MRC-like (MAdCAM-1$^+$) phenotype in response to infection, and that the amount of CXCL13 produced was greater in MRC-like cells than in other FRC populations (MAdCAM-1), as determined by microflow imaging (MFI) (Figures 2H–2J). This is in keeping with our histological staining that indicated that increased CXCL13 production in response to *Hp* is largely associated with cells expressing an MRC-like phenotype.

These observations demonstrate that MRC-like cells strongly increase in number, at least in part due to proliferation, and that they appear within more central locations following infection. Thus, these cells are likely to serve as an important source of CXCL13 at IFRs and in the T cell-rich paracortical zone. In keeping with the previously reported role for CXCR5$^+$ DCs in promoting the T helper 2 response development following *Hp* infection (León et al., 2012), we found that the increase in CXCL13-expressing cells located at the IFR correlated with increased accumulation of DCs in close association with ER-TR7$^+$ fibers (Figure S2E). The IFR is also known to be the site where antigen-activated B cells position themselves to receive T cell help (Garside et al., 1998; Wang et al., 2015). Thus, CXCL13 production by interfollicular MRC-like cells is likely to play an important role in the T cell-DC interactions that are known to be important in driving T helper 2 responses. Based on these observations, we next focused on defining the events that regulate the development of CXCL13$^+$ MRC-like cells within the IFR of the mLN following infection.

IL-4Rα Signaling to B Cells Is Required for the Expansion of CXCL13-Producing MRC-like Cells following *Hp* Infection

Recent work from our laboratory has indicated that IL-4Rα signaling is necessary for the expansion of FRCs and the generation of new B cell follicles following *Hp* infection (Dubey et al., 2016). To determine whether this pathway was also necessary for the development of MRC-like cells within the IFR, we examined the mLNs from naive or infected wild-type (WT) and interleukin-4 receptor α knockout (IL-4Rα$^{-/-}$) mice. Naive mLNs from both groups of mice exhibited a similar localization of MRC-like cells, with the majority of these cells present within a reticular layer of the peripheral cortical zone, just beneath the SCS with no sign of their presence at IFR (Figure 3A). As expected, *Hp* infection led to a significant enlargement of the mLN as measured by total weight and cellularity and the development of MRC-like cells within the cortical and paracortical follicular mantle and/or IFR in WT mice; however, both parameters were markedly reduced in IL-4Rα$^{-/-}$ mice (Figures 3B–3D). To further confirm a requirement for IL-4Rα signaling in the *Hp*-induced development of MRC-like cells, we enumerated these cells by flow cytometry. Both the percentage of live cells that were positive for FRC markers (CD45$^-$CD35$^-$CD31$^-$PDPN$^+$MAdCAM-1$^-$) or MRC markers (CD45$^-$CD35$^-$CD31$^-$PDPN$^+$MAdCAM-1$^+$) and the total number of these two cell populations were significantly reduced in IL-4Rα$^{-/-}$ animals compared to WT mice following infection (Figures 3E–3G). These results present a previously unidentified function for IL-4Rα signaling in driving the development of reticular cells in the IFR and paracortical region into one that expresses an MRC phenotype following infection.

To gain insight into which cells expressing IL-4Rα upon *Hp* infection promote the expansion of MRC-like cells within the IFR of the cortex and the paracortex, we generated bone marrow (BM) chimeras using WT or IL-4Rα$^{-/-}$ BM cells adoptively transferred into lethally irradiated WT or IL-4Rα$^{-/-}$ hosts. Under naive conditions, the selective absence of IL-4Rα on radioresistant stromal cells (WT → IL-4Rα$^{-/-}$ chimeras) or on radiosensitive hematopoietic cells (IL-4Rα$^{-/-}$ → WT chimeras) had little impact on the location of cells expressing MRC markers, with these cells largely restricted to the SCS of both sets of mice (Figure 4A). Following *Hp* infection, WT → IL-4Rα$^{-/-}$ chimeras harbored increased numbers of MRC-like cells with a distribution similar to that seen in WT mice (Figures 4B–4D). By contrast, the absence of IL-4Rα on radiosensitive cells (IL-4Rα$^{-/-}$ → WT chimeras) resulted in a reduced number of MRC-like cells present in the IFR or in the paracortex (Figures 4B–4D). CXCL13 expression was found to be enriched in MRC-like cells present in the paracortex of WT → IL-4Rα$^{-/-}$ chimeras, but not IL-4Rα$^{-/-}$ → WT chimeras (Figures S3A and S3B) following infection.

We and others have previously shown that IL-4Rα-expressing B cells play an important role in driving protective immunity against helminths (McCoy et al., 2008; Wojciechowski et al., 2009), and we had previously hypothesized that IL-4Rα signaling directly to B cells is important for driving FRC expansion and remodeling within the mLN (Dubey et al., 2016). To determine whether IL-4-activated B cells were also driving the development of CXCL13$^+$ MRC-like cells, we generated mixed BMCs mice in which only B cells lacked IL-4Rα expression (JhT$^{-/-}$ + IL-4Rα$^{-/-}$ → WT chimeras) and compared these mice to their control counterparts (JhT$^{-/-}$ + WT → chimeras). In uninfected mice, the presence or absence of IL-4Rα on B cells did not influence the existence of MRC-like cells adjacent to the SCS of mLNs (Figure 5A). However, following *Hp* infection, their development within the paracortical region and IFR was

(A and B) mLN cryosections from naive (A) and 21 dpi (B) were stained for MRCs and visualized by their expression of RANKL (red), MAdCAM-1 (green), and PDPN (gray). Scale bar, 100 μm. Right-hand insets show higher-magnification pictures of the interfollicular region (IFR). All of the images are representative of three or more independent experiments, each including n ≥ 3–5 mice per group per time point.

(C and D) The total weight (C) and total cellularity (D) of WT and IL-4Rα$^{-/-}$ mice mLNs at naive 12 and 21 dpi. Data are pooled from two independent experiments and represent means ± SEMs.

(E) Fluorescence-activated cell sorting (FACS) plots showing MRCs within the mLNs of infected WT and IL-4Rα$^{-/-}$ mice.

(F) Live cells that were TER119$^-$CD45$^-$CD31$^-$CD35$^-$Podoplanin$^+$MAdCAM-1$^+$ were considered MRCs and TER119$^-$CD45$^-$CD31$^-$CD35$^-$Podoplanin$^+$MAdCAM-1$^-$ were considered FRCs and are presented as the percentage of live cells.

(G) Histogram representing the absolute numbers of mLN FRCs and MRCs quantified using flow cytometry in WT and IL-4Rα$^{-/-}$ at 21 dpi. Data are pooled from two independent experiments and represent means ± SEMs.

Magenta circle, B cell follicle; blunt-end white arrow, paracortical T cell zone; magenta rectangle, IFR. Statistical analyses were performed using non-parametric Mann-Whitney t test and significance denoted as *p < 0.05, **p < 0.01, ***p < 0.001, and ****p < 0.0001.

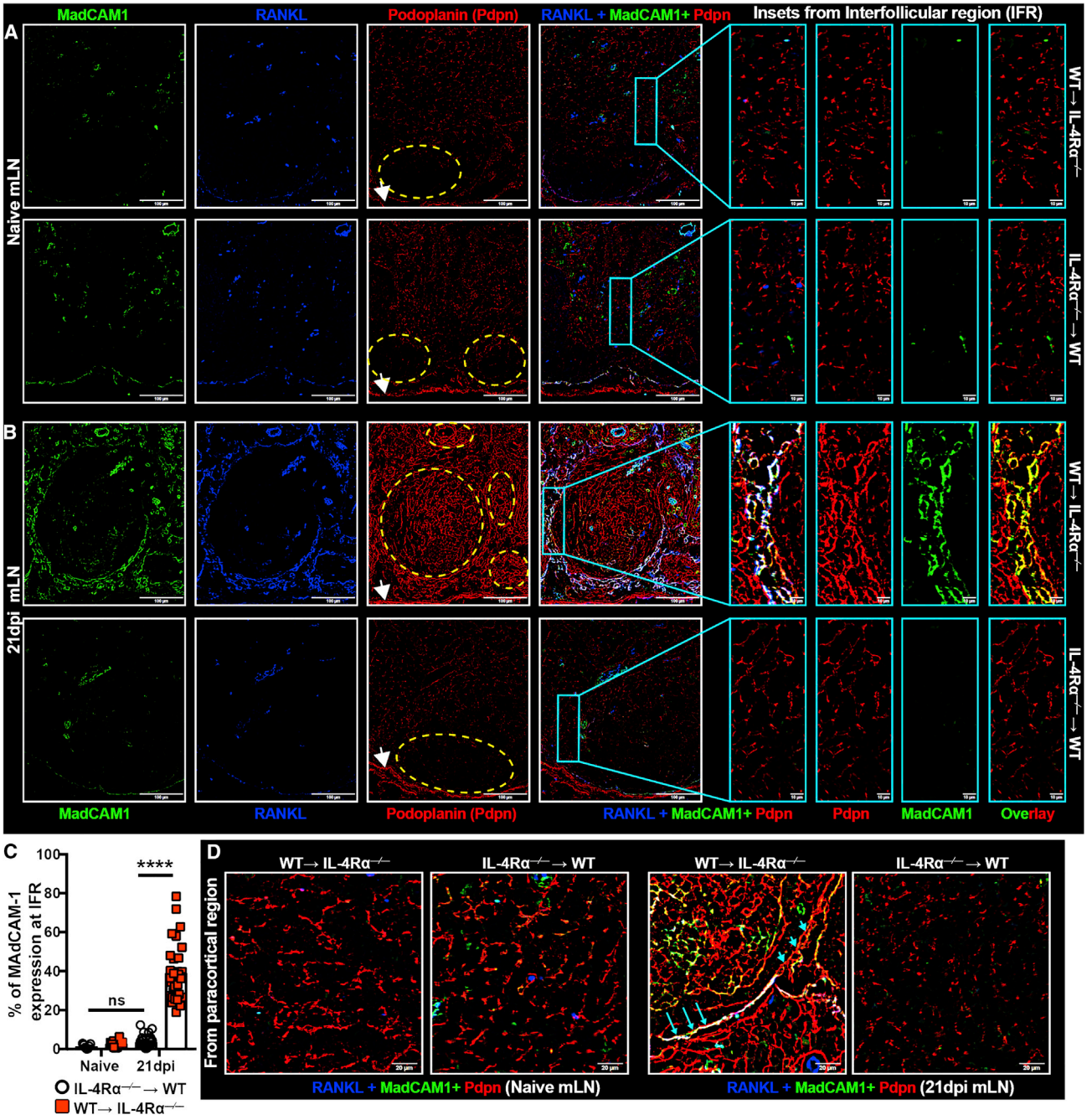

Figure 4. IL-4Rα-Expressing Hematopoietic Cells Are Required for MRC Expansion and Remodeling following Helminth Infection

Bone marrow chimera (BMC) mice (donor strain-recipient strain) were generated using C57BL/6 (WT) and IL-4Rα$^{-/-}$ mice, as described in Method Details. Chimeras lacking IL-4Rα expression on non-hematopoietic cells (WT → IL-4Rα$^{-/-}$) were compared to chimeras lacking IL-4Rα expression exclusively on hematopoietic cells (IL-4Rα$^{-/-}$ → WT). All of the mice were infected with *Hp* and the mLNs collected at day 0 (naive) and 21 dpi and visualized using immunofluorescence microscopy.

(A and B) mLN cryosections from naive (A) and 21 dpi (B) infected BMCs were stained for MRCs identified by the expression of MAdCAM-1 (green), RANKL (blue), and PDPN (red). Scale bar, 100 μm. The capsule, IFR, and B cell follicle are highlighted using a solid white arrow, a cyan rectangle, and dotted yellow circles, respectively. At right are higher-magnification images of the IFR. Scale bars, 100 and 10 μm.

(C) MAdCAM-1 expression within the IFR was quantified by segmenting the images and is presented as the percentage of the total area covered.

(D) Naive and 21 dpi mLN images showing the presence of MRCs within the paracortical regions. Scale bar, 20 μm. MRCs are highlighted by long cyan arrows, and MAdCAM-1^{-} FRCs are highlighted by short cyan arrows. Images are from single mice and are representative of two independent experiments, each including n ≥2–3 mice per group per time point.

Statistical analyses were performed using ANOVA and Bonferroni's multiple comparison test, and significance denoted as ns = not significant and ****$p < 0.0001$.

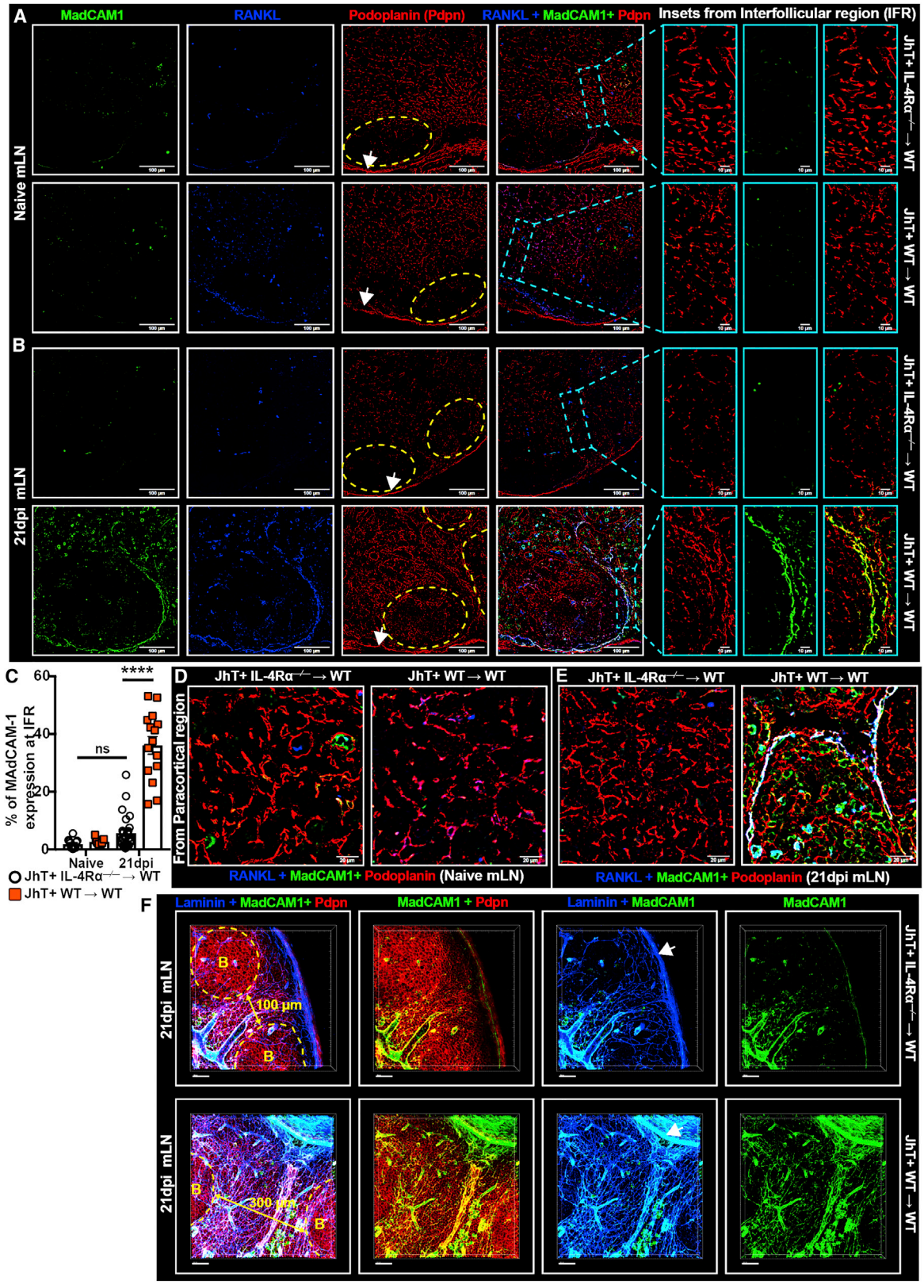

(legend on next page)

disrupted in the case of mice with B cells lacking IL-4Rα expression (Figures 5B–5E). To further validate our observations, we evaluated the presence or absence of MRC-like cells (laminin^{+-} MAdCAM1^{+}PDPN^{+}) within the IFR using thick vibratome sections. We observed a significantly reduced IFR along with reduced numbers of MRC-like cells in the IFR of chimeric mice lacking IL-4Rα on B cells (JhT$^{-/-}$ + IL-4Rα$^{-/-}$ → WT) compared to control chimeras (JhT$^{-/-}$ + WT → WT) following infection (Figure 5F; Video S7). To determine whether IL-4Rα signaling to B cells is also necessary for CXCL13 expression, we examined the mLNs of the same BMCs and observed a clear reduction in *Hp*-induced CXCL13 expression within the IFR of the paracortex when IL-4Rα signaling to B cells was disrupted (Figures S4A and S4-B). Staining of thick vibratome sections confirmed reduced CXCL13 expression in the IFR of chimeric mice lacking IL-4Rα on B cells (JhT$^{-/-}$ + IL-4Rα$^{-/-}$ → WT) compared to control chimeras (JhT$^{-/-}$ + WT → WT) following infection (Figures 6A and 6B). The diminished CXCL13 expression correlated with a significantly reduced number of newly developed B cell follicles (with and without FDCs) in these chimeras (Figures 6C–6F and S4C) and with reduced DC accumulation within the IFRs of both the cortex and the paracortex of infected mice (Figures 6G S4D, and S4E). These observed changes were significant as the loss of IL-4Rα signaling on B cells also resulted in higher worm burdens (Figure 6H). These data demonstrate that IL-4Rα signaling in B cells is necessary for the expansion of CXCL13-producing MRC-like cells within the IFR of mLNs from infected mice. We also observed that the reduced expression of CXCL13-producing MRC-like cells correlates with a reduction in the development of new B cell follicles within the paracortex and with reduced protective immunity.

LTβR Expression by CCL19^{+} Stromal Cells Is Required for the Expansion of CXCL13-Producing MRC-like Cells following *Hp* Infection and Their Appearance within the Paracortex

We have previously shown that *Hp*-induced B cell follicle formation requires IL4Rα-dependent lymphotoxin expression by hematopoietic cells (Dubey et al., 2016), while our findings outlined above showed that the development of both MRC-like cells and new B cell follicles in the paracortex requires IL-4Rα signaling to B cells. Given that IL-4 can upregulate lymphotoxin expression on lymphocytes (Dubey et al., 2016), which then can ligate the LTβR on reticular cells in response to infection (Chai et al., 2013; Dubey et al., 2016), we next assessed whether lymphotoxin expression by B or T cells was necessary for the development of CXCL13-producing MRCs-like cells. To address this question, we created mixed BM chimeras (BMCs) in which B cells (JhT$^{-/-}$ + LTβ$^{-/-}$ → WT) or T cells (TCRβδ$^{-/-}$ + LTβ$^{-/-}$ → WT) were incapable of expressing surface lymphotoxin. Mixed BMCs using WT donors were also generated (JhT$^{-/-}$ + WT → WT and TCRβδ$^{-/-}$ + WT → WT) as controls. WT mice were used as recipients to ensure that the mice had a well-developed lymphoid structure. Naive mLNs of all chimeric mice showed the presence of cells expressing MRC markers in the layer beneath the capsule (Figures S5A and S5B). The absence of lymphotoxin on B cells but not T cells resulted in the reduced development of MRC-like cells in the infected mice (Figures S5C and S5D), which most likely accounted for reduced CXCL13 expression at the IFR (Figures S5E–S5G, magenta insets). A higher-magnification view further confirmed that CXCL13^{+} cells penetrated into the B cell follicle (Figure S5F) in response to *Hp* infection, as seen previously. Of note, the loss of MRC-like cells in mice lacking lymphotoxin on B cells, but not T cells, also resulted in reduced CXCL13 production in both FDC^{+} and FDC^{-} follicles following infection (Figures S5H–S5J). Overall, these results demonstrate that lymphotoxin expression by B cells is necessary for the expansion of CXCL13-producing MRC-like cells within the IFR of mLN from infected mice.

We have previously shown that lymphotoxin-producing B cells drive the expansion of FRCs that express LTβR using CCL19-Cre-mediated LTβR ablation on these cells (Dubey et al., 2016). We used this system to address whether the infection-induced development of CXCL13^{+} MRC-like cells was also driven by LTβR signaling to FRCs. We first validated the previously reported CCL19 promoter-driven expression of Cre on various fibroblast subsets, including MRCs present in the SCS of naive mice (Fasnacht et al., 2014). We achieved this by crossing the CCL19-Cre line to a line of mice expressing enhanced yellow fluorescent protein (eYFP) from the *Rosa26* locus (*Rosa26*-eYFP). An immunohistological analysis for the expression of eYFP was combined with PDPN and MAdCAM-1, which is expressed by SCS cells expressing MRC markers. Cre-mediated activity was observed in both MAdCAM-1^{+}PDPN^{+} cells (MRCs) and MAdCAM-1^{-}PDPN^{+} cells, with the latter comprising T cell zone FRCs (Figures S6A and S6B). The

Figure 5. B Cell Expression of IL-4Rα Is Required for MRC Expansion and Remodeling following Helminth Infection

Mixed BMC mice were generated using JhT$^{-/-}$ plus C57BL/6 (WT) or IL-4Rα$^{-/-}$-deficient donors and C57BL/6 (WT) recipients as described in Method Details. Chimeras lacking IL-4Rα expression exclusively on B cells (JhT$^{-/-}$ + IL-4Rα$^{-/-}$) were compared to control mice having WT B cells (JhT$^{-/-}$ + WT). All of the mice were infected with *Hp* and the mLN collected at day 0 (naive) and 21 dpi were stained for MAdCAM-1 (green), RANKL (blue), and PDPN (red) to identify MRCs network. Montage images were acquired and presented for individual and combined channels.

(A and B) Images showing single and combined immunofluorescence staining from the cortical regions of naive (A) and infected (B) mLNs are shown. Scale bar, 100 μm. The capsule, IFR, and B cell follicle are highlighted using a solid white arrow, a dotted cyan rectangle, and dotted yellow circles, respectively. Higher-magnification images of the insets are shown on the right. Scale bar, 10 μm.

(C) MAdCAM-1 expression within the IFR was quantified by segmenting the images and is presented as the percentage of the total area covered by MAdCAM-1-expressing cells.

(D and E) Images showing paracortical regions from (D) naive and (E) infected mice. Scale bar, 20 μm. All of the images were representative of two independent experiments. Each independent experiment included n ≥ 2–3 mice per group per time-point.

(F) Thick vibratome sections of chimeric mice were stained for laminin, MAdCAM-1, and PDPN to visualize the presence of MRCs at IFR. The increase in IFR was also seen as depicted using a yellow arrow. See also Videos S5 and S6.

Statistical analyses were performed using ANOVA and Bonferroni's multiple comparison test, and significance denoted as ns = not significant and ****$p < 0.0001$.

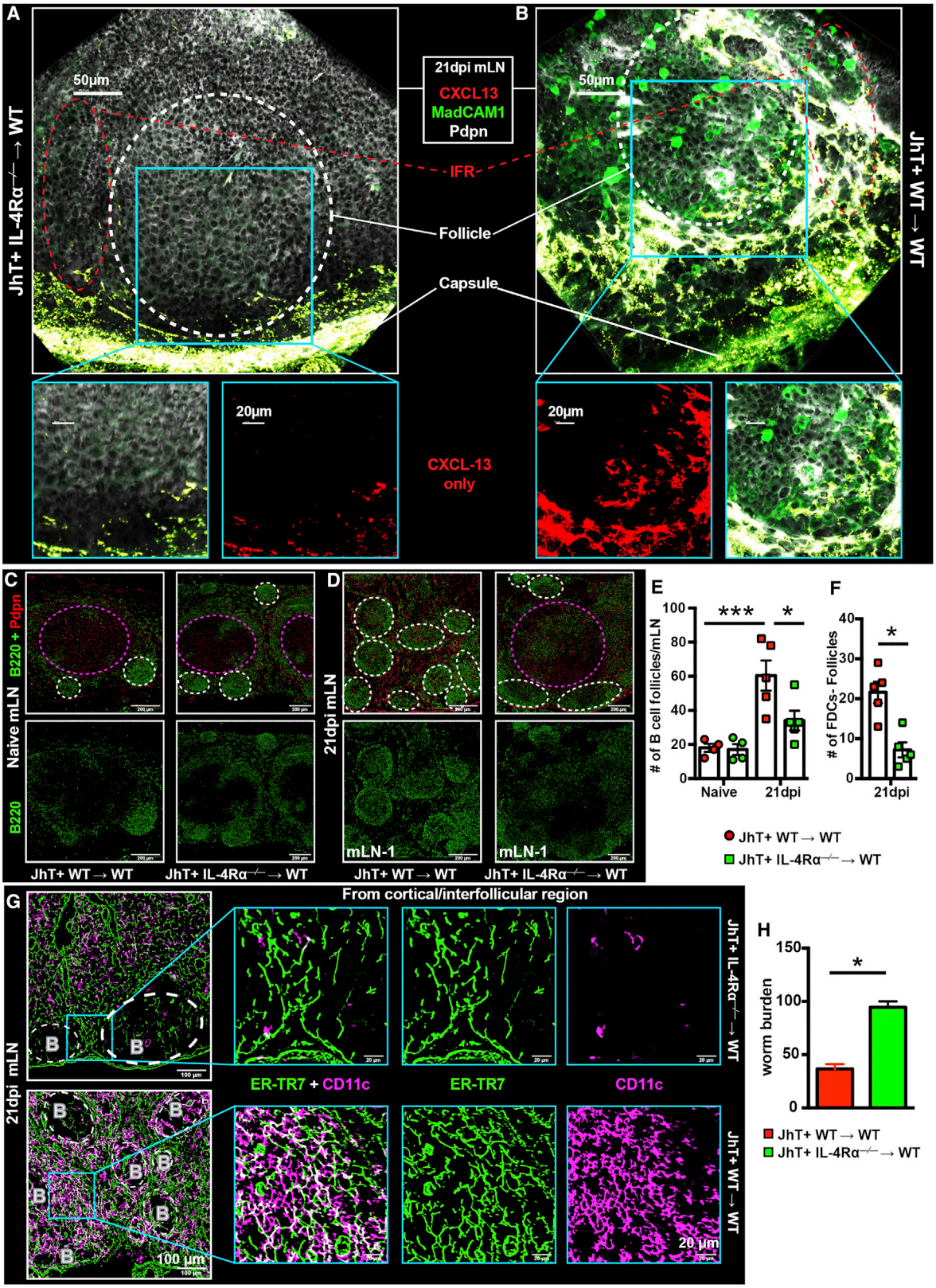

(legend on next page)

MAdCAM-1$^+$ cells seen in the paracortex are mainly HEVs, which were negative for eYFP expression and showed positive staining for CXCL13, as described previously (Kanemitsu et al., 2005) (Figure S6B, yellow inset, and Figure S6C, cyan arrowheads). Based on these results, we concluded that the *Ccl19-cre* transgene targets both MAdCAM-1$^+$ MRCs and T cell zone FRCs, but not MAdCAM-1$^+$ HEVs. To assess the contribution of LTβR signaling to the development of FRC subsets under naive conditions, we performed an immunohistological analysis on mLNs from CCL19-Cre mice crossed to LTβR$^{fl/fl}$ mice. We could easily identify the cells expressing MRC markers in the layer beneath the SCS region in mice lacking LTβR on CCL19^{Cre+} cells and in their WT littermate controls (data not shown), along with very low CXCL13 expression within the paracortical region (Figure S6C, yellow insets). Infection with *Hp* resulted in a dramatic remodeling of the stromal network and the development of CXCL13-producing MRC-like cells within the IFRs of the cortical and paracortical region of LTβR$^{+/+}$ mice, but not in LTβR$^{fl/fl}$ (Figures S6C–S6E, S7A, and S7B), indicating that infection-induced expansion and/or differentiation of CXCL13-producing MRC requires LTβR signaling to fibroblasts. Whether the infection-induced CXCL13-producing MRC-like cells develop from pre-existing SCS MRCs, T zone FRCs, or precursor FRCs is unclear. However, the reduced number of MAdCAM-1$^+$CXCL13$^+$ MRC-like cells observed in infected LTβR$^{fl/fl}$ mice (Figure S7C) correlated with a significantly reduced number of germinal centers (Figures S7D and S7E).

Resolution and Re-emergence of CXCL13-Producing MRCs following Parasite Clearance and Re-infection

B cells play an important protective role during secondary *Hp* infection (McCoy et al., 2008; Wojciechowski et al., 2009); yet whether the *de novo* B cell follicles observed following primary infection (1°*Hp*) (Dubey et al., 2016) are also apparent during the host response to secondary infection (2°*Hp*) is unknown. To address this, we drug cleared the parasite from infected mice and collected the draining mLNs from mice no longer harboring the parasite and from secondary challenge infected mice at days 12 or 21 post-infection (Figure 7A). The 2°*Hp* infection was followed by a dramatic increase in the number of B cell follicles in the paracortical region and an increase in MRC-like cells in the IFR (Figures 7B and 7C). The number of CXCL13-producing cells within the IFR and mantle regions were also increased following secondary infection (Figures 7D, S7F, and S7G). The newly developed B cell follicles present in primary infected mice resolved following antihelminthic treatment, with very few CXCL13-producing cells observed in the mantle region or the IFR (Figures 7D, S7F, and S7G). Increased CXCL13 expressing MRCs in the IFR correlated with an increase in the number of both FDC$^-$ and FDC$^+$ B cell follicles, with both having comparable CXCL13 expression (Figures 7E–7I). While the number of FDC$^+$ follicles did not change, the number of FDC$^-$ B cell follicles decreased from days 12 to 21 following secondary infection (Figures 7E and 7F). These experiments suggest that cortical stromal remodeling is an active process that can resolve and re-emerge post-recurring inflammation.

These data indicate that cortical region CXCL13-expressing mLN MRCs can expand, proliferate, and remodel along with other lymphoid stromal cells to seed IFR, non-cortical regions for DCs/T and B cells interaction which is important for constructing the microenvironment that may promote the B cell follicle expansion.

DISCUSSION

CXCL13 is an important chemokine with multiple roles in the proper development and organization of secondary lymphoid organs. CXCL13-producing stromal cells function to position immune cells—including B cells, DCs, and follicular T cells—to distinct compartments, and this process is essential for promoting efficient adaptive immune responses (Bénézech et al., 2015; Randall et al., 2008; Reif et al., 2002; Roozendaal and Mebius, 2011; van de Pavert et al., 2009). We have previously reported the expansion and re-localization of FRCs to the mantle of *de novo* B cell follicles following *Hp* infection (Dubey et al., 2016). In the present study, we identify a subset of the FRCs that expand in response to infection and are capable of producing the B cell-attracting chemokine CXCL13. Using deep tissue imaging and by combining various surface markers, we were able to more accurately define the mLN stromal microenvironment of the IFR and paracortical region and observed that the *Hp*-induced CXCL13-producing cell expressed the MRC markers MAdCAM-1 and RANKL. We also demonstrated that IL-4Rα

Figure 6. B Cell Expression of IL-4Rα Is Required for CXCL13 Expression by MRCs

Mixed BMC mice (donor strain/recipient strain) were generated as in Figure 5, and mLNs collected from day 0 (naive) and 21dpi *Hp* infection.

(A and B) Thick vibratome sections from the mLNs of infected chimeric mice (A) lacking IL-4Rα expression exclusively on B cells (JhT$^{-/-}$ + IL-4Rα$^{-/-}$) or (B) having WT cells (JhT$^{-/-}$ + WT) were stained for CXCL13 (red), MAdCAM-1 (green), and PDPN (gray). Montage images were acquired and presented for individual and combined channels. Images from the cortical regions are shown. Scale bar, 50 μm. White dashed lines represent a B cell follicle located near the capsule, and red dashed lines indicate an IFR. Higher magnification images of the cyan insets are shown. Scale bars, 50 and 20 μm.

(C and D) mLN cryosections from (C) naive and (D) 21 dpi chimeric mice were stained for B220 (green) and PDPN (red). The dashed white circles represent B cell follicles and the magenta circles represent T cell zones. All of the images are representative of two independent experiments, each including n ≥ 3 mice per group per time point. Scale bars, 50 and 20 μm.

(E and F) The total number of B cell follicles (E) and FDC$^-$ B cell follicles (not showing an FDC-M1 network) (F) present within the entire mLNs of naive (n = 4) or infected (n = 5) BMCs was counted. Data are pooled from two independent experiments, each including n ≥ 2–3 mice per group per time point.

(G) mLN cryosections from naive and infected chimeric mice lacking IL-4Rα on B cells (JhT$^{-/-}$ + IL- 4Rα$^{-/-}$) and their respective controls (JhT$^{-/-}$ + WT) showing IFR DCs accumulation. CD11c$^+$ (magenta; representing DCs) and ER-TR7$^+$ (green; representing the stromal network) are shown for individual and combined channels. Scale bars, 200 and 20 μm.

(H) The total number of adult parasites in the intestinal lumen of BMC mice were enumerated at 21 dpi and represented as worm burden. Data represent means ± SEMs. Statistical analyses were performed using ANOVA, Bonferroni's multiple comparison test, or Mann-Whitney t test, and significance denoted as *p < 0.05, **p < 0.01, ***p < 0.001, and ****p < 0.0001.

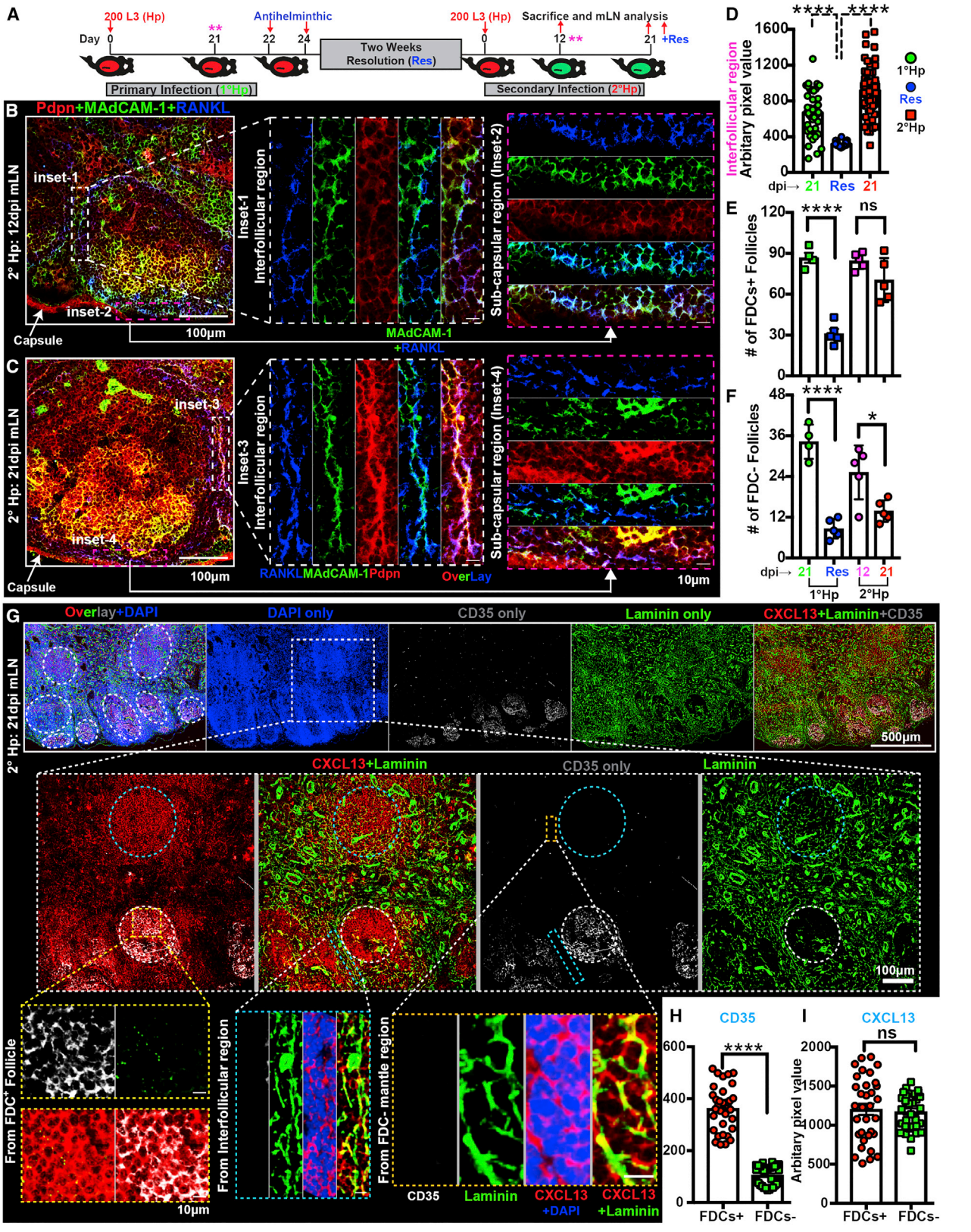

(legend on next page)

signaling to B cells and lymphotoxin signaling to FRCs were required for the development and remodeling of CXCL13$^+$ MRC-like cells. Based on these findings, we can build a model in which IL-4 activation of B cells leads to a B cell-reticular cell interaction, resulting in the expansion and/or differentiation of CXCL13$^+$ MRC-like cells necessary for promoting the adaptive type 2 immune response (Figure S7H).

The differentiation and maturation of specific LN stromal cell subpopulations are thought to require LTβR signaling to stromal organizer cells, which then mature into FDCs, FRCs, or MRCs (Randall et al., 2008; Roozendaal and Mebius, 2011). However, the exact lineage relations between these different cell types remain unclear (Roozendaal and Mebius, 2011). Fate mapping studies indicate that MRCs can give rise to FDCs during B cell follicle development (Jarjour et al., 2014). We observed that the increase in CXCL13-producing MRC-like cells in the IFR region of *Hp*-infected mice correlated with the formation of both FDC$^-$ and FDC$^+$ B cell follicles. This indicates that the development of new B cell follicles may be partially driven by the MRC-like cells along with FDCs.

Whether the increased numbers of CXCL13$^+$ MRCs identified in the IFR of infected mLNs arise from precursor stromal cells or CXCL13$^-$ FRCs, or whether they represent existing SCS MRCs that proliferate and migrate to the paracortex is unclear. However, two of our observations together support our model in which existing SCS MRCs can proliferate and seed the IFR: (1) deep tissue image analysis, which reveals a continuous reticular structure from the SCS toward the IFR, and (2) the active proliferation of MRCs. Unfortunately, we were not able to test this hypothetical model, as both SCS MRCs and T cell zone FRCs are positive for CCL19^{Cre}-driven eYFP$^+$ expression in advance of infection (Figure S6) (Fasnacht et al., 2014). New genetic tools targeting distinct populations of LN reticular cells and their precursors will need to be developed to reveal the exact lineage relations between CXCL13-producing cells located in the SCS, IFRs, and paracortical region.

Chemokine-dependent positioning of ILCs, lymphocytes, and DCs within the LN plays an important role in adaptive immunity (Kastenmüller et al., 2013; Mueller and Germain, 2009; Schulz et al., 2016). Protection against *Hp* infection has been previously shown to require CXCL13, which allowed CXCR5$^+$ DCs to accumulate within the IFR as early as 8 days post-infection (dpi) (León et al., 2012). Our work supports these findings and extends them to show that MRC-like cells present in the IFR are likely to be responsible for the accumulation of CXCR5$^+$ DCs, as these two cell types accumulated in the same region. Moreover, CXCL13 production by FDCs was decreased rather than increased by helminth infection, as seen previously in other infection models (Mueller et al., 2007; St John and Abraham, 2009). CXCL13 has been shown to upregulate surface lymphotoxin expression on B cells (Ansel et al., 2000), and the majority of lymphotoxin-producing naive and isotype switched B cells are present at the IFR or mantle region (Dubey et al., 2016). Thus, high CXCL13 expression by MRC-like cells present in these sites would be expected to promote a feed-forward loop and result in further B cell accumulation and activation and further activation of LTβR expressing reticular cells. IL-4, which is largely produced by T helper cells in *Hp*-infected mLNs (King and Mohrs, 2009) and usually peaks between 12 and 21 dpi (Finney et al., 2007; Mosconi et al., 2015), may act as a second feed-forward loop, with IL-4 upregulating lymphotoxin on B cells and thereby promoting CXCL13 production by MRCs in the IFR, eventually leading to the accumulation of more T helper 2-promoting DCs. These results further emphasize the complex interplay between FRCs and DCs, which are already known to contribute to LN expansion (Acton et al., 2014; Chyou et al., 2011; Worbs et al., 2017).

Of note, the findings that MRCs expand and produce CXCL13 raises the possibility that MAdCAM-1 expression by MRCs plays an important role in promoting T helper 2 responses. Both naive and effector lymphocytes in mLNs can express α4β7 integrin, the ligand for MAdCAM-1, and this integrin is crucial for entry from

Figure 7. Magnitude of CXCL13 Production and MRCs Remodeling during Secondary Infection with *Hp*

(A) Schematic of infection scheme in which WT mice were infected with *Hp*, then treated with an antihelminthic drug (cobantril) at 21 dpi and allowed to rest for 2 weeks before challenge infection with 200 infective *Hp* larvae. mLNs were collected from 21 dpi primary infected (1°*Hp*), 12 and 21 dpi secondary infected (2°*Hp*), and 21 dpi mice treated with the antihelminthic drug, sacrificed along with 2°*Hp* 21 dpi mice. mLNs from naive mice treated with the antihelminthic drug were also analyzed.

(B and C) Cryosections from mLN of 12 (B) and 21 (C) dpi 2°*Hp* infected mice were stained and MRCs identified by the expression of MAdCAM-1 (green), RANKL (blue), and PDPN (red). The dashed white rectangles represent IFR (insets 1 and 3), and the magenta rectangles represent the SCS region (insets 2 and 4). The capsule is highlighted using solid arrows. At right, higher-magnification images of the IFR and SCS region insets. All of the images are representative of two independent experiments, each including n ≥ 2–3 mice per group per time point. Scale bars, 100 and 10 μm.

(D) CXCL13 pixel intensities were quantified from mice of the various groups: 1°*Hp* (green circle), 2°*Hp* (magenta and red squares), resolved group (blue circle), and naive control treated with antihelminthic (gray circle). The resolution (Res) group of mice was treated with the antihelminthic drug without challenge infection and were sacrificed on the same day as 2°*Hp* 21 dpi along with naive mice for comparison. Data represent means ± SEMs and are representative of two independent experiments, with n = 3 mice per group and >10 IFR per mouse.

(E and F) FDC$^+$ (E) and FDC$^-$ (F) follicles within the mLN were enumerated. Data represent means ± SEMs. Data were pooled from two independent experiments, each including n ≥ 2–3 mice per group per time point.

(G) Immunofluorescence images showing combined and segmented panels from the mLN of 21 dpi 2°*Hp*-infected mice stained with laminin (green), CXCL13 (red), CD35 (gray), and DAPI (blue). CXCL13 expression at follicular (yellow square), mantle (orange rectangle), and intrafollicular regions (cyan rectangles) are shown at higher magnification. White and cyan dashed-line circles represent FDC$^+$ and FDC$^-$ follicles, respectively.

(H and I) CD35 (H) and CXCL13 (I) expression within FDC$^+$ and FDCs$^-$ follicles were determined as described in Method Details. Data represent means ± SEMs and are representative of two independent experiments with n = 3 mice per group, with >15 follicles analyzed. CD35 expression was significantly higher in FDC$^+$ follicles compared to FDC$^-$ follicles, which had background-level pixels (range, 65–150, presumably due to the low CD35 expression found in B cells relative to FDCs). Statistical analyses were performed using ANOVA, Bonferroni's multiple comparison test or the Mann-Whitney t test, and significance denoted as *p < 0.05, **p < 0.01, ***p < 0.001, and ****p < 0.0001.

the bloodstream into the mLNs and intestinal tissues (Iwata et al., 2004; Miyasaka and Tanaka, 2004; Xu et al., 2010). Our work identifying MAdCAM-1-expressing MRC-like cells in the IFR extends this notion by indicating that the availability of such integrins may also play a role in attracting and retaining various lymphocytes within the IFR of the infected mLN, where DC-T cell interactions are known to take place. The adherence of B cells to MAdCAM-1 under static and flow conditions are known to be CXCL13 dependent (Kanemitsu et al., 2005). MRCs expressing both MAdCAM-1 and CXCL13 in and around the newly formed B cell follicles may thereby retain B cells and promote follicle formation in response to *Hp* infection. The remodeling of the MRC network during infection such that it frames the B cell follicle, not only on the SCS side but also in the paracortex and the IFR, suggests that these cells may also have roles in delivering additional chemokines and antigens directly to the follicle and/or to FDCs (Gonzalez et al., 2009). This notion is supported by previous observations that FRCs can form conduits that deliver antigen both to B cell follicles and to the paracortex (Roozendaal et al., 2009; Sixt et al., 2005). On several occasions, we also observed CXCL13 expression in blood vessels, which is in line with previous reports (Kanemitsu et al., 2005). FRC subsets form very firm contact with MAdCAM1$^+$ HEVs (Herzog et al., 2013), and the presence of an interconnected FRC and MRC reticular network around these vessels may serve as an arresting point for incoming DCs and B and T cells (expressing CXCR5) by providing additional CXCL13. This will help further in cellular activation, which could govern cellular differentiation, trafficking to distinct niches, and follicle formation.

Mionnet et al. (2013) previously noted that after complete Freund's adjuvant injection, B cells migrate out of the follicle to "trespass" into the T cell zone, where they instruct FRCs to produce CXCL13 in an LTβ-dependent manner. In contrast to our findings, these CXCL13$^+$ FRCs did not express RANKL or MAdCAM-1 (indicating they were not MRCs), and the authors instead called these cells versatile stromal cells and hypothesized that either FDCs or versatile stromal cells function to establish B cell follicle identity and to promote B cell retention in the germinal center (Mionnet et al., 2013; Wang et al., 2011). Our study expands on this work to indicate that IL-4-driven inflammation also promotes CXCL13$^+$ production, mainly by MRCs and less by versatile stromal cells or FDCs. These results further suggest great plasticity between various lymphoid stromal cells and/or their precursors, with LTβR signaling being crucial for CXCL13 production, FRC proliferation, and LN expansion (Bénézech et al., 2012; Chai et al., 2013; Cyster, 2014; Fütterer et al., 1998). We could not detect any significant changes in the mLNs of naive WT and LTβR$^{fl/fl}$ mice, with both groups exhibiting more or less similar organization and B cell follicle numbers during homeostasis (Dubey et al., 2016). This is perhaps not surprising, as the LTo that seed the LN anlagen are clearly different between PLN and mLN (Cupedo et al., 2004) and maintain differences in adulthood (Fletcher et al., 2011).

In summary, we have shown that IL-4Rα signaling to B cells following *Hp* infection can promote LTβR signaling to stromal fibroblasts, resulting in the development of CXCL13$^+$ MRC-like cells in the IFRs of the cortex and paracortex of the mLN. The presence of these cells correlated with, and is likely to be important for, the accumulation of CXCR5-expressing DCs at this site; these DCs are known to promote the ensuing Th2 response. These cells may also participate in the formation of the newly developed B cell follicles occurring within this region, and partially replace FDC in this function (Figure S7H). Our findings identify a previously unrecognized role for IL-4Rα signaling in promoting the development of CXCL13-expressing FRC/MRC-like cells and highlight the important role of lymphocyte-stromal cell interactions in maintaining effective adaptive immune responses within the draining LNs.

STAR★METHODS

Detailed methods are provided in the online version of this paper and include the following:

- KEY RESOURCES TABLE
- CONTACT FOR REAGENT AND RESOURCE SHARING
- EXPERIMENTAL MODEL AND SUBJECT DETAILS
  - Animal experiments and ethics statement
- METHOD DETAILS
  - Flow cytometry and antibodies
  - Histology and immunofluorescence microscopy
  - CXCL13 immunofluorescence staining and quantification
  - Vibratome Sections
  - Image acquisition and processing
  - Bone marrow chimeras (BMC)
  - RNA isolation and qRT-PCR analysis
- QUANTIFICATION AND STATISTICAL ANALYSIS

SUPPLEMENTAL INFORMATION

Supplemental Information can be found online at https://doi.org/10.1016/j.celrep.2019.04.079.

ACKNOWLEDGMENTS

We thank the École Polytechnique Fédérale de Lausanne (EPFL) and University of Lausanne (UNIL) animal facility, flow cytometry core facility, Jessica Sordet-Dessimoz, and the histology core facility (HCF-EPFL) for support and expertise. A special thanks to Olivier Burri, Thierry Laroche, and Arne Seitz from the Bio-Imaging and Optics Platform for ImageJ/Fiji tools and crucial advice regarding image analysis. L.K.D. is Chargé de recherche in the Department of Biochemistry, UNIL (DB-UNIL). This work was supported by a grant from DB-UNIL (to L.K.D.), the Leenaards Prize for Translational Research in Medicine, awarded to N.L.H. and S.A.L. by the Leenaards Foundation, Lausanne, Switzerland, and a grant from the Swiss National Science Foundation (31003A-166161 to S.A.L.), Switzerland.

AUTHOR CONTRIBUTIONS

L.K.D. and N.L.H. conceived of and designed the study. L.K.D. performed all of the experiments, analyzed the data, and wrote the paper. B.L. provided CCL19^{-Cre} × LTβR$^{fl/fl}$ mice and critical suggestions throughout the manuscript. S.A.L. contributed Col-1a1GFP mice, various important tools, reagents, resources, and critical suggestions throughout the manuscript. L.K.D. and N.L.H. analyzed the data and wrote the paper.

DECLARATION OF INTERESTS

The authors declare no competing interests.

Received: April 26, 2018
Revised: January 14, 2019
Accepted: April 17, 2019
Published: May 21, 2019

REFERENCES

Acton, S.E., Farrugia, A.J., Astarita, J.L., Mourão-Sá, D., Jenkins, R.P., Nye, E., Hooper, S., van Blijswijk, J., Rogers, N.C., Snelgrove, K.J., et al. (2014). Dendritic cells control fibroblastic reticular network tension and lymph node expansion. Nature *514*, 498–502.

Aguzzi, A., Kranich, J., and Krautler, N.J. (2014). Follicular dendritic cells: origin, phenotype, and function in health and disease. Trends Immunol. *35*, 105–113.

Ansel, K.M., Ngo, V.N., Hyman, P.L., Luther, S.A., Förster, R., Sedgwick, J.D., Browning, J.L., Lipp, M., and Cyster, J.G. (2000). A chemokine-driven positive feedback loop organizes lymphoid follicles. Nature *406*, 309–314.

Ansel, K.M., Harris, R.B.S., and Cyster, J.G. (2002). CXCL13 is required for B1 cell homing, natural antibody production, and body cavity immunity. Immunity *16*, 67–76.

Bénézech, C., Mader, E., Desanti, G., Khan, M., Nakamura, K., White, A., Ware, C.F., Anderson, G., and Caamaño, J.H. (2012). Lymphotoxin-β receptor signaling through NF-κB2-RelB pathway reprograms adipocyte precursors as lymph node stromal cells. Immunity *37*, 721–734.

Bénézech, C., Luu, N.-T., Walker, J.A., Kruglov, A.A., Loo, Y., Nakamura, K., Zhang, Y., Nayar, S., Jones, L.H., Flores-Langarica, A., et al. (2015). Inflammation-induced formation of fat-associated lymphoid clusters. Nat. Immunol. *16*, 819–828.

Chai, Q., Onder, L., Scandella, E., Gil-Cruz, C., Perez-Shibayama, C., Cupovic, J., Danuser, R., Sparwasser, T., Luther, S.A., Thiel, V., et al. (2013). Maturation of lymph node fibroblastic reticular cells from myofibroblastic precursors is critical for antiviral immunity. Immunity *38*, 1013–1024.

Chyou, S., Benahmed, F., Chen, J., Kumar, V., Tian, S., Lipp, M., and Lu, T.T. (2011). Coordinated regulation of lymph node vascular-stromal growth first by CD11c+ cells and then by T and B cells. J. Immunol. *187*, 5558–5567.

Cremasco, V., Woodruff, M.C., Onder, L., Cupovic, J., Nieves-Bonilla, J.M., Schildberg, F.A., Chang, J., Cremasco, F., Harvey, C.J., Wucherpfennig, K., et al. (2014). B cell homeostasis and follicle confines are governed by fibroblastic reticular cells. Nat. Immunol. *15*, 973–981.

Cupedo, T., Vondenhoff, M.F.R., Heeregrave, E.J., De Weerd, A.E., Jansen, W., Jackson, D.G., Kraal, G., and Mebius, R.E. (2004). Presumptive lymph node organizers are differentially represented in developing mesenteric and peripheral nodes. J. Immunol. *173*, 2968–2975.

Cyster, J.G. (2014). Blown away: the unexpected role of lymphotoxin in lymphoid organ development. J. Immunol. *192*, 2007–2009.

Cyster, J.G., and Schwab, S.R. (2012). Sphingosine-1-phosphate and lymphocyte egress from lymphoid organs. Annu. Rev. Immunol. *30*, 69–94.

Dubey, L.K., Lebon, L., Mosconi, I., Yang, C.Y., Scandella, E., Ludewig, B., Luther, S.A., and Harris, N.L. (2016). Lymphotoxin-Dependent B Cell-FRC Crosstalk Promotes De Novo Follicle Formation and Antibody Production following Intestinal Helminth Infection. Cell Rep. *15*, 1527–1541.

Dubey, L.K., Karempudi, P., Luther, S.A., Ludewig, B., and Harris, N.L. (2017). Interactions between fibroblastic reticular cells and B cells promote mesenteric lymph node lymphangiogenesis. Nat. Commun. *8*, 367.

Esser-von Bieren, J., Mosconi, I., Guiet, R., Piersgilli, A., Volpe, B., Chen, F., Gause, W.C., Seitz, A., Verbeek, J.S., and Harris, N.L. (2013). Antibodies trap tissue migrating helminth larvae and prevent tissue damage by driving IL-4Rα-independent alternative differentiation of macrophages. PLoS Pathog. *9*, e1003771.

Fasnacht, N., Huang, H.-Y., Koch, U., Favre, S., Auderset, F., Chai, Q., Onder, L., Kallert, S., Pinschewer, D.D., MacDonald, H.R., et al. (2014). Specific fibroblastic niches in secondary lymphoid organs orchestrate distinct Notch-regulated immune responses. J. Exp. Med. *211*, 2265–2279.

Finney, C.A.M., Taylor, M.D., Wilson, M.S., and Maizels, R.M. (2007). Expansion and activation of CD4(+)CD25(+) regulatory T cells in Heligmosomoides polygyrus infection. Eur. J. Immunol. *37*, 1874–1886.

Fletcher, A.L., Malhotra, D., Acton, S.E., Lukacs-Kornek, V., Bellemare-Pelletier, A., Curry, M., Armant, M., and Turley, S.J. (2011). Reproducible isolation of lymph node stromal cells reveals site-dependent differences in fibroblastic reticular cells. Front. Immunol. *2*, 35.

Fletcher, A.L., Acton, S.E., and Knoblich, K. (2015). Lymph node fibroblastic reticular cells in health and disease. Nat. Rev. Immunol. *15*, 350–361.

Fu, Y.-X., Huang, G., Wang, Y., and Chaplin, D.D. (1998). B lymphocytes induce the formation of follicular dendritic cell clusters in a lymphotoxin α-dependent fashion. J. Exp. Med. *187*, 1009–1018.

Fütterer, A., Mink, K., Luz, A., Kosco-Vilbois, M.H., and Pfeffer, K. (1998). The lymphotoxin β receptor controls organogenesis and affinity maturation in peripheral lymphoid tissues. Immunity *9*, 59–70.

Garside, P., Ingulli, E., Merica, R.R., Johnson, J.G., Noelle, R.J., and Jenkins, M.K. (1998). Visualization of specific B and T lymphocyte interactions in the lymph node. Science *281*, 96–99.

Gonzalez, S.F., Pitcher, L.A., Mempel, T., Schuerpf, F., and Carroll, M.C. (2009). B cell acquisition of antigen in vivo. Curr. Opin. Immunol. *21*, 251–257.

Hardtke, S., Ohl, L., and Förster, R. (2005). Balanced expression of CXCR5 and CCR7 on follicular T helper cells determines their transient positioning to lymph node follicles and is essential for efficient B-cell help. Blood *106*, 1924–1931.

Herzog, B.H., Fu, J., Wilson, S.J., Hess, P.R., Sen, A., McDaniel, J.M., Pan, Y., Sheng, M., Yago, T., Silasi-Mansat, R., et al. (2013). Podoplanin maintains high endothelial venule integrity by interacting with platelet CLEC-2. Nature *502*, 105–109.

Hoorweg, K., Narang, P., Li, Z., Thuery, A., Papazian, N., Withers, D.R., Coles, M.C., and Cupedo, T. (2015). A Stromal Cell Niche for Human and Mouse Type 3 Innate Lymphoid Cells. J. Immunol. *195*, 4257–4263.

Iwata, M., Hirakiyama, A., Eshima, Y., Kagechika, H., Kato, C., and Song, S.-Y. (2004). Retinoic acid imprints gut-homing specificity on T cells. Immunity *21*, 527–538.

Jarjour, M., Jorquera, A., Mondor, I., Wienert, S., Narang, P., Coles, M.C., Klauschen, F., and Bajénoff, M. (2014). Fate mapping reveals origin and dynamics of lymph node follicular dendritic cells. J. Exp. Med. *211*, 1109–1122.

Junt, T., Scandella, E., and Ludewig, B. (2008). Form follows function: lymphoid tissue microarchitecture in antimicrobial immune defence. Nat. Rev. Immunol. *8*, 764–775.

Kanemitsu, N., Ebisuno, Y., Tanaka, T., Otani, K., Hayasaka, H., Kaisho, T., Akira, S., Katagiri, K., Kinashi, T., Fujita, N., et al. (2005). CXCL13 is an arrest chemokine for B cells in high endothelial venules. Blood *106*, 2613–2618.

Kastenmüller, W., Brandes, M., Wang, Z., Herz, J., Egen, J.G., and Germain, R.N. (2013). Peripheral prepositioning and local CXCL9 chemokine-mediated guidance orchestrate rapid memory CD8+ T cell responses in the lymph node. Immunity *38*, 502–513.

Katakai, T., Suto, H., Sugai, M., Gonda, H., Togawa, A., Suematsu, S., Ebisuno, Y., Katagiri, K., Kinashi, T., and Shimizu, A. (2008). Organizer-like reticular stromal cell layer common to adult secondary lymphoid organs. J. Immunol. *181*, 6189–6200.

King, I.L., and Mohrs, M. (2009). IL-4-producing CD4+ T cells in reactive lymph nodes during helminth infection are T follicular helper cells. J. Exp. Med. *206*, 1001–1007.

León, B., Ballesteros-Tato, A., Browning, J.L., Dunn, R., Randall, T.D., and Lund, F.E. (2012). Regulation of T(H)2 development by CXCR5+ dendritic cells and lymphotoxin-expressing B cells. Nat. Immunol. *13*, 681–690.

Luther, S.A., Ansel, K.M., and Cyster, J.G. (2003). Overlapping roles of CXCL13, interleukin 7 receptor alpha, and CCR7 ligands in lymph node development. J. Exp. Med. *197*, 1191–1198.

Mackley, E.C., Houston, S., Marriott, C.L., Halford, E.E., Lucas, B., Cerovic, V., Filbey, K.J., Maizels, R.M., Hepworth, M.R., Sonnenberg, G.F., et al. (2015). CCR7-dependent trafficking of RORγ$^+$ ILCs creates a unique microenvironment within mucosal draining lymph nodes. Nat. Commun. *6*, 5862.

Magri, G., Miyajima, M., Bascones, S., Mortha, A., Puga, I., Cassis, L., Barra, C.M., Comerma, L., Chudnovskiy, A., Gentile, M., et al. (2014). Innate lymphoid cells integrate stromal and immunological signals to enhance antibody production by splenic marginal zone B cells. Nat. Immunol. *15*, 354–364.

McCoy, K.D., Stoel, M., Stettler, R., Merky, P., Fink, K., Senn, B.M., Schaer, C., Massacand, J., Odermatt, B., Oettgen, H.C., et al. (2008). Polyclonal and specific antibodies mediate protective immunity against enteric helminth infection. Cell Host Microbe *4*, 362–373.

Mionnet, C., Mondor, I., Jorquera, A., Loosveld, M., Maurizio, J., Arcangeli, M.-L., Ruddle, N.H., Nowak, J., Aurrand-Lions, M., Luche, H., and Bajénoff, M. (2013). Identification of a new stromal cell type involved in the regulation of inflamed B cell follicles. PLoS Biol. *11*, e1001672.

Miyasaka, M., and Tanaka, T. (2004). Lymphocyte trafficking across high endothelial venules: dogmas and enigmas. Nat. Rev. Immunol. *4*, 360–370.

Mosconi, I., Dubey, L.K., Volpe, B., Esser-von Bieren, J., Zaiss, M.M., Lebon, L., Massacand, J.C., and Harris, N.L. (2015). Parasite Proximity Drives the Expansion of Regulatory T Cells in Peyer's Patches following Intestinal Helminth Infection. Infect. Immun. *83*, 3657–3665.

Mueller, S.N., and Germain, R.N. (2009). Stromal cell contributions to the homeostasis and functionality of the immune system. Nat. Rev. Immunol. *9*, 618–629.

Mueller, S.N., Hosiawa-Meagher, K.A., Konieczny, B.T., Sullivan, B.M., Bachmann, M.F., Locksley, R.M., Ahmed, R., and Matloubian, M. (2007). Regulation of homeostatic chemokine expression and cell trafficking during immune responses. Science *317*, 670–674.

Ohl, L., Henning, G., Krautwald, S., Lipp, M., Hardtke, S., Bernhardt, G., Pabst, O., and Förster, R. (2003). Cooperating mechanisms of CXCR5 and CCR7 in development and organization of secondary lymphoid organs. J. Exp. Med. *197*, 1199–1204.

Okada, T., Ngo, V.N., Ekland, E.H., Förster, R., Lipp, M., Littman, D.R., and Cyster, J.G. (2002). Chemokine requirements for B cell entry to lymph nodes and Peyer's patches. J. Exp. Med. *196*, 65–75.

Randall, T.D., Carragher, D.M., and Rangel-Moreno, J. (2008). Development of secondary lymphoid organs. Annu. Rev. Immunol. *26*, 627–650.

Reif, K., Ekland, E.H., Ohl, L., Nakano, H., Lipp, M., Förster, R., and Cyster, J.G. (2002). Balanced responsiveness to chemoattractants from adjacent zones determines B-cell position. Nature *416*, 94–99.

Roozendaal, R., and Mebius, R.E. (2011). Stromal cell-immune cell interactions. Annu. Rev. Immunol. *29*, 23–43.

Roozendaal, R., Mempel, T.R., Pitcher, L.A., Gonzalez, S.F., Verschoor, A., Mebius, R.E., von Andrian, U.H., and Carroll, M.C. (2009). Conduits mediate transport of low-molecular-weight antigen to lymph node follicles. Immunity *30*, 264–276.

Schiffer, L., Worthmann, K., Haller, H., and Schiffer, M. (2015). CXCL13 as a new biomarker of systemic lupus erythematosus and lupus nephritis - from bench to bedside? Clin. Exp. Immunol. *179*, 85–89.

Schulz, O., Hammerschmidt, S.I., Moschovakis, G.L., and Förster, R. (2016). Chemokines and Chemokine Receptors in Lymphoid Tissue Dynamics. Annu. Rev. Immunol. *34*, 203–242.

Sixt, M., Kanazawa, N., Selg, M., Samson, T., Roos, G., Reinhardt, D.P., Pabst, R., Lutz, M.B., and Sorokin, L. (2005). The conduit system transports soluble antigens from the afferent lymph to resident dendritic cells in the T cell area of the lymph node. Immunity *22*, 19–29.

St John, A.L., and Abraham, S.N. (2009). Salmonella disrupts lymph node architecture by TLR4-mediated suppression of homeostatic chemokines. Nat. Med. *15*, 1259–1265.

Tomer, R., Ye, L., Hsueh, B., and Deisseroth, K. (2014). Advanced CLARITY for rapid and high-resolution imaging of intact tissues. Nat. Protoc. *9*, 1682–1697.

van de Pavert, S.A., Olivier, B.J., Goverse, G., Vondenhoff, M.F., Greuter, M., Beke, P., Kusser, K., Höpken, U.E., Lipp, M., Niederreither, K., et al. (2009). Chemokine CXCL13 is essential for lymph node initiation and is induced by retinoic acid and neuronal stimulation. Nat. Immunol. *10*, 1193–1199.

Wang, X., Cho, B., Suzuki, K., Xu, Y., Green, J.A., An, J., and Cyster, J.G. (2011). Follicular dendritic cells help establish follicle identity and promote B cell retention in germinal centers. J. Exp. Med. *208*, 2497–2510.

Wang, G.-Z., Cheng, X., Zhou, B., Wen, Z.-S., Huang, Y.-C., Chen, H.-B., Li, G.-F., Huang, Z.-L., Zhou, Y.-C., Feng, L., et al. (2015). The chemokine CXCL13 in lung cancers associated with environmental polycyclic aromatic hydrocarbons pollution. eLife *4*, e09419.

Wang, C., Wu, K., Yu, Q., Zhang, S., Gao, Z., Liu, Y., Ni, L., Cheng, Y., Guan, Z., Shi, M., et al. (2016). CXCL13, CXCL10 and CXCL8 as Potential Biomarkers for the Diagnosis of Neurosyphilis Patients. Sci. Rep. *6*, 33569.

Wojciechowski, W., Harris, D.P., Sprague, F., Mousseau, B., Makris, M., Kusser, K., Honjo, T., Mohrs, K., Mohrs, M., Randall, T., and Lund, F.E. (2009). Cytokine-producing effector B cells regulate type 2 immunity to H. polygyrus. Immunity *30*, 421–433.

Worbs, T., Hammerschmidt, S.I., and Förster, R. (2017). Dendritic cell migration in health and disease. Nat. Rev. Immunol. *17*, 30–48.

Xu, B., Cook, R.E., and Michie, S.A. (2010). $\alpha 4\beta 7$ integrin/MAdCAM-1 adhesion pathway is crucial for B cell migration into pancreatic lymph nodes in nonobese diabetic mice. J. Autoimmun. *35*, 124–129.

STAR★METHODS

KEY RESOURCES TABLE

REAGENT or RESOURCE	SOURCE	IDENTIFIER
Antibodies		
Rat anti mouse B220-biotin (Clone RA3-6B2)	Life Technologies	Cat No# RM2615
Rat anti mouse B220 (Clone RA3-6B2)	BioLegend	Cat No# 103202
Armenain hamster anti mouse CD3 (Clone 145-2C11)	BioLegend	Cat No# 100302
Rat anti mouse CD35 (Clone 8C12)	BD PharMingen	Cat No# 558768
Rat anti mouse ER-TR7	BMA Biomedicals	Cat No# T-2109
Rat anti mouse FDCM1	BD PharMingen	Cat No# 551320
Armenain hamster anti mouse CD11c (Clone N418)	BioLegend	Cat No# 117308
Rat anti mouse GL-7-biotin	eBiosciences	Cat No# 13-5902-85
Rat anti mouse IgD (Clone 11-26c)	Southern Biotech	Cat No# 1120-01
Rabbit anti mouse laminin	Sigma-Aldrich	Cat No# L9393
Syrian hamster anti mouse podoplanin (clone 8.1.1)	Hybridoma	N/A
Rat anti mouse CD254 (Clone IKK22/5)-Biotin	eBiosciences	Cat No# 13-5952-82
Rabbit anti mouse RANKL	Peprotech	Cat No# 500-P63
Goat anti mouse CXCL13	R&D Systems	Cat No# AF470
Goat IgG Control	R&D Systems	Cat No# AB-108-C
Rat anti mouse MAdCAM1 (Clone MECA 367)	BioLegend	Cat No# 120702
Goat anti armenian hamster-Alexa 594	Jackson Immuno Research	Cat No# 127-585-160
Donkey anti Rabbit IgG-Alexa 488	Thermo Fischer	Cat No# A21206
Donkey anti Rabbit IgG-Alexa 568	Thermo Fischer	Cat No# A10042
Donkey anti Rabbit IgG-Alexa 647	Thermo Fischer	Cat No# A31573
Donkey anti Rat IgG-Alexa 488	Thermo Fischer	Cat No# A21208
Goat anti Rat IgG-Alexa 568	Thermo Fischer	Cat No# A11077
Donkey anti Rat IgG-biotin	Jackson Immuno Research	Cat No# 712-065-153
Donkey anti Rat IgG-Alexa 647	Jackson Immuno Research	Cat No# 712-605-150
Chicken anti Rat IgG-Alexa 647	Thermo Fischer	Cat No# A-21472
Goat anti Syrian hamster IgG-Alexa 488	Jackson Immuno Research	Cat No# 107-545-142
Goat anti Syrian hamster IgG-Alexa 647	Jackson Immuno Research	Cat No# 107-606-142
Rabbit anti Syrian hamster IgG-Alexa 647	Jackson Immuno Research	Cat No# 307-605-003
Donkey anti Goat IgG-biotin	Jackson Immuno Research	Cat No# 705-035-003
Rat anti mouse-CD45	Biolegend	Cat No# 103114
Rat anti mouse-CD45	Biolegend	Cat No# 103122
Rat anti mouse-CD45	Biolegend	Cat No# 103126
Rat anti mouse-CD31	Biolegend	Cat No# 102422
Rat anti mouse-CD31	Biolegend	Cat No# 102408
Rat anti mouse-CD35	Biolegend	Cat No# 123407
Rat anti mouse-CD35	Biolegend	Cat No# 123408
Rat anti mouse-CD35	Biolegend	Cat No# 123413
Syrian hamster anti mouse Podoplanin	eBiosciences	Cat No# 50-5381
Rat anti mouse-TER119	Biolegend	Cat No# 116215
Rat anti mouse-MAdCAM1	Biolegend	Cat No# 120706
Rat anti mouse-MAdCAM1	Biolegend	Cat No# 120708

(*Continued on next page*)

Continued

REAGENT or RESOURCE	SOURCE	IDENTIFIER
Biological Samples		
Normal mouse serum	Naive mouse (C57BL/6)	N/A
Normal donkey serum	Millipore	S30-100 mL
Chemicals, Peptides, and Recombinant Proteins		
Paraformaldehyde	Merck-Millipore	Cat No# 104005
Collagenase P	Roche	Cat No# 11215809103
Dispase	Roche	Cat No# 04942078001
DNase I	Roche	Cat No# 11284932001
Agarose, low gelling temperature	Sigma Aldrich	Cat No# A9414
(Ethylenedinitrilo)tetraacetic acid (EDTA)	Applichem	Cat No# A4892
DAPI	Sigma Aldrich	Cat No# D9542
Streptavidin-Alexa 488	Molecular Probes	Cat No# S-11223
Streptavidin-Alexa 568	Molecular Probes	Cat No# S-11226
Streptavidin-Alexa 568	Molecular Probes	Cat No# S-21374
ProLong^{TM}Gold Antifade Mountant	ThermoFisher	Cat No# P36934
Tyramide signal amplification kit (Alexa 488 and Alexa 568)	ThermoFisher	Cat No# T20932/34
Streptavidin HRP	Jackson Immunosearch	Cat No# 016-030-084
Cobantril	McCoy et al., 2008	N/A
Tissue-Tek optimum cutting temperature compound (OCT)	Fisher Scientific	Cat No# 14-373-65
Acetone for HPLC, $\geq$ 99.9%	Sigma Aldrich	Cat No# 270725
Critical Commercial Assays		
Light Cycler 480 SYBR Green I Master mix	Roche	Cat No# 04707516001
Depleting anti-CD45 microbeads	Miltenyi Biotech	Cat No# 130-052-301
Depleting anti-TER119 microbeads	Miltenyi Biotech	Cat No# 130-049-901
Direct-zol RNA MiniPrep kit	Zymo Research	Cat No# R2051
RevertAid First Strand cDNA Synthesis Kit	ThermoFisher	Cat No# K1622
Experimental Models: Organisms/Strains		
Mouse: C57BL/6 (WT)	Charles River	Strain code: 027
Mouse: JhT knockout	Dubey et al., 2016	N/A
Mouse: IL-4Rα knockout	Dubey et al., 2016	N/A
Mouse: LT-β knockout	Dubey et al., 2016	N/A
Mouse: TCR-$\beta\delta$ knockout	Dubey et al., 2016	N/A
Mouse: C57BL/6N-Tg(Ccl19-Cre)(*Ccl19-Cre*)	Chai et al., 2013	N/A
Mouse: *Ltbr*$^{fl/fl}$	Chai et al., 2013; Dubey et al., 2017	N/A
Mouse: *Rosa26*-eYFP	Jackson Laboratories	Stock No: 006148
Parasite: *Heligmosomoides polygyrus (Hp)*	Dubey et al., 2016	Dubey et al., 2016
Oligonucleotides		
Primer for RT PCR Forward (*Cxcl13*): CATAGATCGGATTCAAGT	This paper	N/A
Primer for RT PCR Reverse (*Cxcl13*): TCTTGGTCCAGATCACAA	This paper	N/A
Primer for RT PCR Forward (*Gapdh*): GTGCCAGCCTCGTCCCG	This paper	N/A
Primer for RT PCR Reverse (*Gapdh*): TTGCCGTGAGTGGAGTCA.	This paper	N/A

(*Continued on next page*)

Continued

REAGENT or RESOURCE	SOURCE	IDENTIFIER
Software and Algorithms		
BD FACS Diva 8	BD Biosciences	http://www.bdbiosciences.com/us/instruments/research/software/flow-cytometry-acquisition/bd-facsdiva-software/m/111112/overview
FlowJo Versions 10	Tree Star	https://www.flowjo.com/solutions/flowjo/downloads/previous-versions
Zeiss ZEN 2010	Carl Zeiss	https://www.zeiss.com/microscopy/int/products/microscope-software/zen-lite.html
GraphPad Prism 7.0	GraphPad	https://www.graphpad.com/scientific-software/prism/
Imaris Versions 8	Bitplane	https://imaris.oxinst.com/packages
Olympus slide scanner software (OlyVIA v.2.6)	Olympus	https://www.olympus-lifescience.com/en/microscopes/virtual/vs120/
Image-J software	Open source	Image-J NIH
VSI reader action bar	EPFL BioImaging & Optics Platform (BIOP)	EPFL BioImaging & Optics Platform (BIOP)
FIJI tools, action bar and analysis	EPFL BioImaging & Optics Platform (BIOP)	EPFL BioImaging & Optics Platform (BIOP)
Other		
ZEISS Lightsheet Z.1 Microscope	Carl Zeiss	https://www.zeiss.com/microscopy/int/products/imaging-systems/lightsheet-z-1.html
VS120 Virtual Slide Microscope	Olympus	https://www.olympus-lifescience.com/en/microscopes/virtual/vs120/
X-CLARITY System for Tissue Clearing	Logos Biosystems	https://logosbio.com/tissue-clearing_3d-imaging/tissue-clearing/x-clarity

CONTACT FOR REAGENT AND RESOURCE SHARING

Further information and requests for resources and reagents should be directed to and will be fulfilled by the Lead Contact, Nicola Harris (nicola.harris@monash.edu).

EXPERIMENTAL MODEL AND SUBJECT DETAILS

Animal experiments and ethics statement

C57BL/6J (WT) mice were obtained from Charles River. Jht $^{-/-}$, IL-4R$\alpha^{-/-}$ mice were bred and maintained on the C57BL/6J background under specific pathogen-free (SPF) conditions at École Polytechnique Fédérale de Lausanne (EPFL), Switzerland. Ccl19^{cre} × LTβR$^{+/+}$ (LTβR$^{+/+}$) and Ccl19^{-cre} × LTβR$^{fl/fl}$ (LTβR$^{fl/fl}$) were provided by Burkhard Ludewig, Kantonsspital St. Gallen and were maintained on the C57BL/6 J background under specific pathogen-free (SPF) conditions at Ecole Polytechnique Federale de Lausanne (EPFL), Switzerland. During the course of study, all the mice (male and females having age in between 8 to 12 weeks) were infected orally with 200 L3 stage *Hp*. Mice were sacrificed at 12 days post-infection (12dpi) or 21 days post-infection (21dpi). Challenge infections (Secondary *Hp*; 2°*Hp*) were performed as previously described (Esser-von Bieren et al., 2013), with slight modifications (see Figure 7A). Briefly, worms were cleared by treating mice with two doses of anthelminthic drug; Cobantril (Interdelta - Givisiez, Fribourg, Switzerland) 21 days after primary infection. 14 days later mice were challenge-infected with 200 L3 stage *Hp*. Mice were sacrificed on day 12 (2°*Hp*-12dpi) and 21 post challenge infection (2°*Hp*-21dpi) and mLNs were collected for analysis. A group of infected mice were treated with cobantril, then left unchallenged and sacrificed on day 60 (equivalent to 2°*Hp* 21dpi) as controls. All animal experiments were approved by the Service de la consommation et des affaires vétérinaires (1066 Épalinges, Canton of Vaud, Switzerland) with the authorization numbers VD 2238.1 and VD 3001.

METHOD DETAILS

Flow cytometry and antibodies

For flow cytometric analysis, mLN were processed as previously described (Dubey et al., 2016). For lymphocyte staining mLN single cell suspensions were gently dispersed, cells filtered through 40-μm-cell strainer, counted and used for FACS staining. For stromal cell staining mLN were subjected to enzymatic digestion using a digestion mixture comprised of RPMI- 1640 containing Dispase and Collagenase P (both from Roche), and 0.1 mg/ml DNase I (Invitrogen). Then cells were resuspended in FACS buffer (PBS containing

2% FBS and 5 mM EDTA). For staining cells and were incubated for 30 min with antibodies against the indicated markers and the samples acquired on BD-LSRII machine and data analyzed using FlowJo (v10.0.6). Various stromal populations were identified using a gating strategy as described previously (Dubey et al., 2016; Fletcher et al., 2011). Briefly, the CD45, CD35 and TER119 negative fractions that were positive for podoplanin (PDPN) and CD31 were identified as LECs, $PDPN^+$ and $CD31^-$ MAdCAM-1 were paracortical FRCs and $PDPN^+$ MAdCAM-1^+ and $CD31^-$ were MRCs. A detailed list of antibodies used is provided in the key resources table (see STAR Methods).

Histology and immunofluorescence microscopy

The entire length of the mLN chain was carefully dissected, weighed, imaged and embedded in Tissue-Tek optimum cutting temperature compound (OCT) (Thermo Scientific), then frozen in an isopentane dry ice bath. Serial cryostat sections (8 μm in thickness) were collected over a span of 400 μm depth on Superfrost/Plus glass slides (Fisher Scientific), air-dried and fixed for 10-15 min in ice-cold acetone. After rehydration in PBS, sections were blocked with 1% (wt/vol) BSA and 1%–4% (vol/vol) normal mouse and donkey serum. Immunofluorescence staining was performed using antibodies diluted in PBS containing 1% (wt/vol) BSA and 1% (vol/vol) normal mouse serum. Sections were incubated with primary antibodies overnight at 4°C. The following day sections were washed three times in PBS and primary antibodies were detected by incubating sections with fluorescently labeled secondary antibodies, and nuclei counterstained with DAPI prior to mounting of the sections using ProLong® anti-fade reagents (Life technologies). Stained sections were then imaged after 24 hr. A detailed list of antibodies used is provided in the key resources table (see STAR Methods).

CXCL13 immunofluorescence staining and quantification

CXCL13 immunofluorescence staining was performed using goat-anti mouse CXCL13 antibody (R&D systems, AF470) as described previously (Mionnet et al., 2013; Schiffer et al., 2015; Wang et al., 2016). CXCL13 antibody was diluted (10-15 μg/ml) in PBS containing 1% (wt/vol) BSA and 1% (vol/vol) normal mouse serum and 4% donkey serum. Sections were incubated with the desired panel mix of MRCs markers along with anti-CXCL13 antibodies overnight at 4°C. The following day sections were washed three times in PBS and probed with donkey anti-goat biotin, rabbit anti-Syrian hamster and donkey anti-rat antibody. Sections were incubated at room temperature (RT) and then washed three to five times in PBS and probed with streptavidin-HRP for 1 hour at RT followed by revelation using Tyramide Signal Amplification (TSA) kit (Invitrogen). Nuclei counter-stained with DAPI prior to mounting of the sections using ProLong® anti-fade reagents (Life technologies). On some occasion's sections were incubated with CXCL13 antibody alone and probed with secondary antibody followed by desired panel mix of MRCs/FRCs/FDCs markers. For thick vibratome sections, 25-50 μg/ml of CXCL13 antibody (AF470) was used in a blocking buffer containing 0.1% Triton X-100 where samples were incubated for at least 5-7 days at 4°C followed by corresponding secondary antibody. The sections were revealed using streptavidin-488/568 as appropriate. On some occasion's sections were revealed using donkey anti-goat alexa 488/568 antibody. On some occasions, CXCL13 pixel intensity was also measured from a pre-defined region of interest (ROI; follicle, mantle, IFR) using Fiji common drawing tools. Various regions of interest (ROI) were then subjected to a defined measure tool to obtain the various pixel intensity across the various groups. To validate the strength of such measure tool CD35, laminin, CXCL13 and DAPI mean pixel intensity were measured across various ROI. FDC^+ follicles had higher pixel values for CD35 (ranging from 250 to 600) whereas FDC- follicles had background level pixels (ranging from 50 to 140). Laminin showed a higher pixel intensity in T cell zone as well as at IFR and mantle region. A positive signal for laminin within the follicle was also seen which most probably be due to presence of B zone reticular cells within the follicle. DAPI remain consistent across the various region analyzed. The low and high pixel values along with background levels were variable across the different experiments, different batch of antibodies and storage time of sections (freshly cut versus stored at −80°C). Therefore, Naive and infected lymph node which were sectioned, stained and imaged on the same day with the same batch of reagents and antibodies were used for such quantification to avoid any batch variations and results were presented as an arbitrary pixel value.

Vibratome Sections

Isolated mLN were fixed overnight at 4°C in freshly prepared 1%–2% paraformaldehyde in PBS, washed and embedded in 2% (w/v) low-melting agarose (Sigma-Aldrich) in PBS. ≈100-200 μm thick sections were cut with a vibratome (Microm HM 650V) and were used for staining. These thick sections were blocked with blocking buffer (as described above) overnight and stained for at 2 to 5 days with the primary antibodies followed by extensive washing in PBS before incubation with fluorescently labeled secondary antibodies. After staining, samples were cleared as described previously (Dubey et al., 2017; Tomer et al., 2014). Briefly, after hydrogel embedding, polymerization was performed for three hours at 37°C followed by washing twice with 1X- PBS. After washing, the samples were subjected to passive clearing using X-CLARITY electrophoretic tissue clearing system (Logos Biosystems) according to the manufacturer recommendations. Completion of tissue clearing was assessed by assessing for transparency using a black and white sheet. On some occasions tissue were cleared by serially incubating in 10–15 mL of 20%, 40% and 60% (wt/vol) fructose, each for 6–8 h in 15 mL conical tubes with gentle rotation at 25°C. Samples were then incubated in 80% (wt/vol) fructose for 12 h, 100% (wt/vol) fructose for 12-18 h and finally in SeeDB (80.2% wt/wt fructose) for 24 h with gentle shaking. After clearing, vibratome sections were imaged using a light sheet microscope (Zeiss) or LSM700/710 upright confocal microscope with 20 × objective. The 3D reconstruction and movies were made using IMARIS (Bitplane).

Image acquisition and processing

Images were acquired on an Olympus VS120-SL full slide scanner using a 20x/0.75 air objective and an OlympusXM10 B/W camera or LSM710 laser scanning confocal microscope or with light sheet microscope (Zeiss) with 20 × objective. For images that were acquired using Olympus VS120-SL full slide scanner or with LSM710 laser scanning confocal microscope, each image was acquired using the indicated fluorescent channels and the same exposure time employed across different samples. The images were downsampled when extracted using the VSI reader action bar developed by the EPFL BioImaging & Optics Platform (BIOP) and were then subjected to the analysis pipeline available through ImageJ/Fiji. For the generation of the final images comparing different samples (i.e., naive versus infected mLN), each fluorescent channel was set to the same brightness and contrast, the mLN chain outlined using Fiji, then assembled such that the final image represented the individual and overlay of all channels. Alternatively, images were directly processed using Olympus slide scanner software (OlyVIA v.2.6) after adjusting the brightness and contrast settings so that they remained the same across all samples compared. For quantitative measurements, immunofluorescence images from naive and infected mice mLN were acquired and segmented using Image-J software and the number of pixels specific for given marker against DAPI was measured using an automated macro and expressed as the percentage of total pixels in each area occupied by given marker.

Bone marrow chimeras (BMC)

Bone marrow (BM) from donor-mice was obtained from the femur and tibia by crushing bones with a mortar. BM cells were injected into C57BL/6j (WT) or IL-4R$\alpha^{-/-}$ recipient mice previously irradiated two times with 450 rad in a 4 h interval. All mice were maintained in specific pathogen-free conditions. For the generation of mixed bone marrow chimeras B cells lacking IL-4Rα expression (B-IL-4R$\alpha^{-/-}$) and B-WT chimeras, C57BL/6J recipients were reconstituted with 80% JhT bone marrow plus 20% IL-4R$\alpha^{-/-}$ bone marrow or with 80% JhT bone marrow plus 20% WT bone marrow respectively. For the generation of mice lacking lymphotoxin expression on B cells (B-*LT*$\beta^{-/-}$) and B-WT chimeras, WT recipients were reconstituted with 80% JHt bone marrow plus 20% *LT*$\beta^{-/-}$ bone marrow or with 80% JHt bone marrow plus 20% WT bone marrow, respectively. For the generation of mice lacking lymphotoxin expression on T cells (T-*LT*$\beta^{-/-}$) and T-WT chimeras, WT recipients were reconstituted with 80% TCR-$\beta\delta$ bone marrow plus 20% *LT*$\beta^{-/-}$ bone marrow or with 80% TCR-$\beta\delta$ bone marrow plus 20% WT bone marrow. Mice received the antibiotic 'Baytril 10%' (1/1,000) in the drinking water for 4 to 8 weeks following bone marrow reconstitution and were subjected to parasite infection at 8 weeks following reconstitution.

RNA isolation and qRT-PCR analysis

The complete length of mLN were collected into trizol and stored at −80°C until used. Stromal and cellular fraction were separated as described previously (Add Nat comm ref 2017). Briefly, mLN were mashed through a 40-μm cell strainer filter using a 5 mL syringe plunger, with the filtered cells representing the soluble cellular part and the remaining white matter left on strainer representing the stromal fraction. RNA was extracted with a Direct-zol RNA MiniPrep kit (Zymo Research) and reverse transcribed using RevertAid cDNA synthesis reagents (Thermo Scientific) for qPCR analysis. qPCR was performed using SYBR Green I Master Mix (Eurogentec) on an Applied Biosystems 7900HT System. The following primers were used to detect chemokines. *Cxcl13* Fw: CATAGATCGGATTC AAGT, *Cxcl13* Rv: TCTTGGTCCAGATCACAA, *Gapdh* Fw GTGCCAGCCTCGTCCCG, *Gapdh* Rv: TTGCCGTGAGTGGAGTCA.

QUANTIFICATION AND STATISTICAL ANALYSIS

Statistical analyses were performed using a non-parametric Mann Whitney Student's t test, one-way or two-way ANOVA as indicated and with post-tests as appropriate. P values indicated as $p < 0.05$ (*), $p < 0.01$ (**), $p < 0.001$ (***), $p < 0.0001$ (****) or ns (statistically not significant). Graph generation and statistical analyses were performed using Prism version 7 (MacOS) software (Graph pad, La Jolla, CA).